THE JOURNAL OF BIOLOGICAL CHEMISTRY VOL. 288, NO. 27, pp. 19986–20001, July 5, 2013

α-Hemoglobin-stabilizing Protein (AHSP) Perturbs the Proximal Heme Pocket of Oxy-α-hemoglobin and Weakens the Iron-Oxygen Bond*[S]

Received for publication, November 18, 2012, and in revised form, May 20, 2013 Published, JBC Papers in Press, May 21, 2013, DOI 10.1074/jbc.M112.437509

Claire F. Dickson[‡], Anne M. Rich[§], William M. H. D'Avigdor[¶], Daniel A. T. Collins[‡], Jason A. Lowry[¶], Todd L. Mollan[‖], Eugene Khandros[**], John S. Olson[‖], Mitchell J. Weiss[**], Joel P. Mackay[¶], Peter A. Lay[§], and David A. Gell[‡1]

*From the [‡]Menzies Research Institute Tasmania, University of Tasmania, Hobart, TAS 7000, Australia, [§]School of Chemistry, University of Sydney, NSW 2006, Australia, [¶]School of Molecular Bioscience, University of Sydney, NSW 2006, Australia, [‖]Department of Biochemistry and Cell Biology, Rice University, Houston, Texas 77251, and **Cell and Molecular Biology Group, University of Pennsylvania, Philadelphia, Pennsylvania 19104*

Background: α-Hemoglobin stabilizing protein (AHSP) is a hemoglobin chaperone.
Results: AHSP causes a subtle perturbation of the proximal heme pocket of O_2-α-hemoglobin, lengthening the Fe-O_2 bond and enhancing O_2 dissociation.
Conclusion: Pro-30 in wild-type AHSP promotes αHb autooxidation by introducing strain into the proximal heme pocket.
Significance: αHb·AHSP complexes are intermediates in Hb assembly and achieve αHb detoxification.

α-Hemoglobin (αHb)-stabilizing protein (AHSP) is a molecular chaperone that assists hemoglobin assembly. AHSP induces changes in αHb heme coordination, but how these changes are facilitated by interactions at the αHb·AHSP interface is not well understood. To address this question we have used NMR, x-ray absorption spectroscopy, and ligand binding measurements to probe αHb conformational changes induced by AHSP binding. NMR chemical shift analyses of free CO-αHb and CO-αHb·AHSP indicated that the seven helical elements of the native αHb structure are retained and that the heme Fe(II) remains coordinated to the proximal His-87 side chain. However, chemical shift differences revealed alterations of the F, G, and H helices and the heme pocket of CO-αHb bound to AHSP. Comparisons of iron-ligand geometry using extended x-ray absorption fine structure spectroscopy showed that AHSP binding induces a small 0.03 Å lengthening of the Fe-O_2 bond, explaining previous reports that AHSP decreases αHb O_2 affinity roughly 4-fold and promotes autooxidation due primarily to a 3–4-fold increase in the rate of O_2 dissociation. Pro-30 mutations diminished NMR chemical shift changes in the proximal heme pocket, restored normal O_2 dissociation rate and equilibrium constants, and reduced O_2-αHb autooxidation rates. Thus, the contacts mediated by Pro-30 in wild-type AHSP promote αHb autooxidation by introducing strain into the proximal heme pocket. As a chaperone, AHSP facilitates rapid assembly of αHb into Hb when βHb is abundant but diverts αHb to a redox resistant holding state when βHb is limiting.

Adult human hemoglobin (Hb)[2] is a tetramer of two αHb and two βHb subunits. The αHb and βHb chains share a common fold, and each binds a single, iron-containing protoporphyrin IX (heme) molecule in a deep pocket, protected from solvent. The central iron atom in each heme is the site of physiological dioxygen (O_2) binding. α-Hemoglobin stabilizing protein (AHSP) is a molecular chaperone that binds free αHb in a heterodimeric complex (see Fig. 1*A*) (1–3) and is essential for normal erythropoiesis (4–12).

One role of AHSP is to protect erythroid cells from oxidative damage arising from the action of the heme iron in free αHb (6). In aqueous solutions containing air-equilibrated buffer, the Fe(II) atoms of heme groups spontaneously oxidize to the ferric (Fe(III)) state, which results in the production of superoxide anions. This process is termed autooxidation. Autooxidation is inhibited by the physicochemical properties of the heme pocket that allow reversible oxygen binding. However, spontaneous oxidation is not blocked completely, and the superoxide anions generated undergo rapid enzymatic and non-enzymatic disproportionation to H_2O_2 and O_2. H_2O_2 is a key mediator of oxidative stress that can react with either reduced or oxidized globins to produce highly reactive ferryl or oxo-ferryl (Fe(IV)) heme groups (13, 14), and subsequent reactions lead to destruction of Hb as well as production of potent pro-oxidants that damage membranes and other cellular components (15–17). Additionally, autooxidation to the ferric state renders Hb incapable of O_2

* This work was supported, in whole or in part, by National Institutes of Health (NIH) Grants HL47020, GM35649, and HL110900 (all to J. S. O.) and Institute of Biosciences and Bioengineering NIH Biotechnology Predoctoral Training Grant GM008362 (to T. L. M.). This work was also supported by the Australian Research Council (ARC) (to P. A. L., J. P. M., and D. A. G.), an ARC Australian Professorial Fellowship (to P. A. L.), a National Health and Medical Research Council Senior Research Fellowship (to J. P. M.), and Robert A. Welch Foundation Grant C-0612 (to J. S. O. and T. L. M.).
[S] This article contains supplemental Tables 1–3.
[1] To whom correspondence should be addressed: Menzies Research Institute Tasmania, University of Tasmania, 17 Liverpool St., Hobart, TAS 7000, Australia. Tel.: 61-3-62264608; E-mail: david.gell@utas.edu.au.

[2] The abbreviations used are: Hb, hemoglobin; AHSP, α-hemoglobin stabilizing protein; $AHSP^{P30A}$, AHSP with a Pro-30 to Ala substitution; EXAFS, extended X-ray absorption fine structure; r.m.s., root mean square; e.s.d., estimated standard deviation; SEC, size exclusion chromatography; MS, multiple scattering; pMB, *p*-hydroxymercuribenzoate; XANES, x-ray absorption near edge structure; HSQC, heteronuclear single quantum correlation

transport and greatly enhances the rates of hemin loss and globin denaturation.

Compared with mature Hb, isolated αHb and βHb chains produce higher levels of reactive oxygen species (18–20), presumably linked to a loss of structural integrity of the heme pocket. Oxidative damage occurs in erythroid cells of β-thalassaemic mice that contain elevated levels of unpaired αHb (21–24). Kong *et al.* (6) showed similar increases in reactive oxygen species in $AHSP^{-/-}$ mice, suggesting that AHSP has a role in limiting reactive oxygen species production during normal erythropoiesis. In a purified system AHSP inhibits the reaction of Fe(III) αHb with H_2O_2 (2, 20), and recently Mollan *et al.* (20) demonstrated that AHSP binding prevents the production of Fe(IV)═O heme and associated protein radicals when Fe(III) αHb is exposed to H_2O_2.

The low reactivity of Fe(III) αHb in the presence of AHSP correlates with a change in αHb heme pocket structure. In native Hb, the αHb heme group is coordinated through a single His-87 side chain, termed the proximal histidine (see Fig. 1*B*), allowing exogenous ligands in the distal heme pocket to interact with iron. In the ferric αHb·AHSP complex, Fe(III) becomes coordinated by both the proximal and distal histidine side chains (bis-histidyl heme coordination; see Fig. 1*C*) (1, 2, 11, 25–27). Coordination of low-spin Fe(III) with six strong ligands blocks the binding of exogenous ligands and associated electron transfer reactions involving oxygen species. The switch from native to bis-histidyl heme coordination is accompanied by a change to a non-native αHb tertiary structure (r.m.s deviation of 3.3 Å over 135 C^{α} atoms), which dissociates from AHSP ~100-fold slower than Fe(II) αHb (20, 25, 27).

As well as inducing changes in the structure of Fe(III) αHb, AHSP binding causes a >10-fold increase in the autooxidation rate of Fe(II) αHb (11, 20, 25, 28, 29), also resulting in formation of bis-histidyl Fe(III) αHb. To understand how promoting αHb autooxidation is compatible with reduced reactive oxygen species production in erythroid cell, it is important to appreciate that repeated movement between different iron oxidation states can occur for a single heme group, and this redox cycling increases the probability of irreversible changes in the globin and other cellular components. In contrast, autooxidation of αHb to the bis-histidyl αHb structure dramatically lowers the Fe(III)/Fe(II) redox potential (20) and inhibits interactions with exogenous ligands, thus inhibiting redox cycling. However, the structural mechanism by which AHSP accelerates αHb autooxidation and, more generally, how AHSP promotes the protective bis-histidyl structure is not well understood.

Previous work from our group has suggested that AHSP induces strain into the O_2-αHb structure that is relieved upon autooxidation by reorganization of the αHb protein fold (25). Mutation of Pro-30 to Ala ($AHSP^{P30A}$) in loop 1 of AHSP (Fig. 1*A*) leads to an ~4-fold reduction in αHb·AHSP autooxidation rates, suggesting that Pro-30 contributes to the strained conformation. However, how contacts at the αHb·AHSP interface are transmitted to the αHb heme pocket and the nature of the strained O_2-αHb structure are unknown. Difficulties in characterizing the O_2-αHb·AHSP complex arise from its propensity to spontaneously convert to a bis-histidyl structure. A previous x-ray crystallographic study suggested that the strained

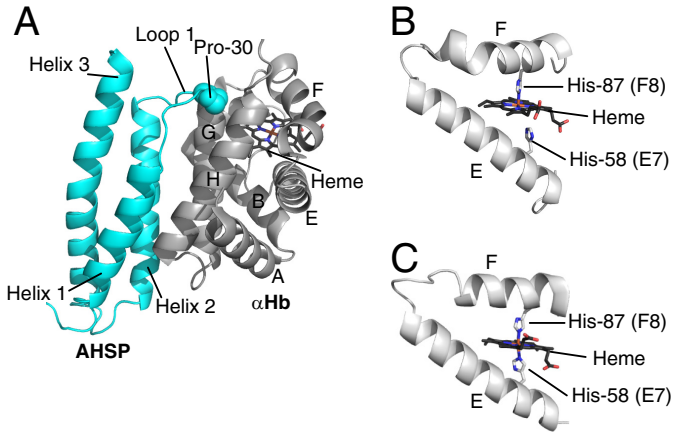

FIGURE 1. **Structure of the bis-histidyl αHb·AHSP complex.** *A*, shown is a schematic of the αHb·AHSP complex (PDB 3IA3). Loop 1 and Pro-30 (*spheres*) of AHSP are positioned at the interface with αHb. *B*, shown are the E-F helices of αHb in the native conformation, as seen in the deoxy Hb complex (PDB 2DN2) (53), with His-87 (His F8) coordinating the heme iron. His-58 (His E7) sits away from the iron site and regulates the binding of diatomic ligands. *C*, in a complex formed from AHSP and met-αHb (PDB 3IA3), His-87 and His-58 simultaneously coordinate the Fe(III) heme iron (bis-histidyl heme coordination).

O_2-αHb structure involved large-scale changes in the globin polypeptide structure and heme coordination geometry (1).

To explore these issues, we have used NMR and EXAFS to probe the complexes of CO- and O_2-liganded αHb with AHSP in solution. The results show that the tertiary structure of CO/O_2-αHb in these complexes closely resembles that of CO/O_2-αHb in the native HbA tetramer and, therefore, that our previous model of O_2-αHb·AHSP (1) is unlikely to represent the initial AHSP binding event in solution. We show that mutation of Pro-30 in AHSP leads to NMR chemical shift perturbations in the F-helical region of CO-αHb, and the concomitant changes in O_2 and CO binding reactivity help identify how this strain introduced into the proximal portion of the heme pocket promotes autooxidation of O_2-αHb.

EXPERIMENTAL PROCEDURES

Protein Production—The structured region, residues 1–90 of human AHSP, and mutants thereof were expressed and purified as described previously (25). CO-αHb was purified from human blood (3). O_2-αHb was generated by gently blowing oxygen across the surface of CO-αHb under a concentrated 10-watt halogen light source. The procedure was carried out on ice, and the formation of the O_2-αHb was monitored by UV-visible spectroscopy (Shimadzu UV-1601). Isotopically labeled αHb for NMR studies was co-expressed with βHb and methionine aminopeptidase in *Escherichia coli* from the previously described plasmid pHE7 (30). Expression was carried out in the *E. coli* strain JM109. One liter of overnight culture in DM-4 minimal media as described by Looker *et al.* (31) containing D-glucose (5 g $liter^{-1}$), NH_4Cl (0.7 g $liter^{-1}$), thiamine (30 mg $liter^{-1}$), ampicillin (100 mg $liter^{-1}$), and trace metal solution (32) was inoculated into a final volume of 3.5 liters of DM-4 medium containing thiamine (30 mg $liter^{-1}$), ampicillin (100 mg $liter^{-1}$), trace metal solution, yeast extract (50 μl of 10% w/v solution), and antifoam (Sigma) in a 5-liter fermentor vessel (New Brunswick BioFlo). Growth was maintained at 37 °C, pH

6.8, with aeration and monitored in real time based on dissolved O_2 concentration. The culture exhausted the nitrogen supply at an absorbance of ~1 (600 nm) and was provided with 2 g of $^{15}NH_4Cl$. The culture exhausted the glucose supply at an absorbance of ~3, and 1.5 g of D-[U(99%)-^{13}C]glucose was provided, and the temperature was shifted to 32 °C. The addition of a further 2 g of $^{15}NH_4Cl$, 1.5 g of D-[U(99%)-^{13}C]glucose occurred at an absorbance of ~3.5, and expression was induced with 0.2 mM isopropyl β-D-1-thiogalactopyranoside and 15 μM hemin. Cells were collected by centrifugation after 5 h, and the resulting cell pellets were washed once in 10 mM Tris-HCl, 0.5 mM EDTA, pH 8.0. Cell pellets were resuspended in the same buffer and saturated with CO before lysis by sonication (Ultrasonic Processor 500 W, Sonics & Materials Inc.). After clarification by centrifugation, recombinant Hb was purified as previously described (33). The Hb chains were split by the addition of a 2-fold molar excess (per cysteine) of *p*-hydroxymercuribenzoate (pMB) and purified as previously described (3).

Size Exclusion Chromatography (SEC) and In-line Light Scattering—SEC chromatography was carried out on a 24-ml Superose 12 column (GE Healthcare) in 0.1 M sodium phosphate, pH 7.0 (21 °C). Protein concentrations were determined based on UV-visible absorbance. The concentrations of AHSP and mutants thereof were obtained after unfolding in 6 M guanidine-HCl using molar extinction coefficients calculated based on the amino acid compositions (34). CO/O_2-αHb concentrations were determined based on absorption peaks arising from $\pi \rightarrow \pi^*$ transitions in the porphyrin ring using molar extinction coefficients for the corresponding CO/O_2 forms of Hb (35). The weight-average molecular weight (M_w) of particles in solution was determined directly from measurements of light scattering and protein concentration (36). In-line light scattering measurements were made at 41.5°, 90.0°, and 138.5° with respect to the incident beam using a mini-DAWN with 690 nm laser (Wyatt Technology Corp., Santa Barbara CA), calibrated against toluene. Protein concentrations were determined based on the refractive index measured by an Optilab differential refractometer (Wyatt Technology Corp.) calibrated against NaCl standards. Molecular weight calculations were performed for each 50-μl fraction across the elution peaks using the ASTRA software (Wyatt Technology Corp.) with the assumption of a standard value for the specific refractive index increment with respect to sample concentration (dn/dC) of 0.19 ml g^{-1}. The presence of the heme and pMB groups upon the value of dn/dC was neglected in this case.

NMR Spectroscopy—All NMR spectroscopic measurements were conducted using a Bruker Avance II 600 MHz spectrometer equipped with a triple-resonance TCI cryoprobe (Bruker, Karlsruhe, Germany), then processed using Topspin 2.1 (Bruker), and analyzed using SPARKY 3.1 (37). Samples were formulated as described, with the addition of 20 μM 4,4-dimethyl-4-silapentane-1-sulfonic acid (DSS) and 5% D_2O. Backbone assignments were made using HNCA, HNCACB, CBCA(CO)NH, and ^{15}N-edited NOESY according to standard assignment strategies. His side chain resonances were assigned based on ^{15}N-HSQC, ^{15}N-NOESY-HSQC, and two-dimensional TOCSY (two-dimensional total correlation spectroscopy)/NOESY spectra. Tautomer/charge state was inferred for His side chains from cross-peak intensities in the ^{15}N-HSQC (38). Spectra were recorded at sample temperatures of 15 and 25 °C for αHb and αHb·AHSP complexes, respectively, to optimize spectral quality.

EXAFS—Samples for x-ray absorption spectroscopy were prepared in 20 mM sodium phosphate buffer, pH 7.0 (21 °C), with 30% sucrose (0.88 M) as the cryoprotectant. Sucrose was the preferred cryoprotectant, as it caused minimal changes in the UV-visible spectrum. The O_2-αHb·AHSP complex was formed by mixing O_2-αHb with a 1.1 molar excess of AHSP. Final protein concentrations were 6 and 2.5 mM for O_2-αHb and O_2-αHb·AHSP samples, respectively. The solutions were injected into 140-μl Lucite XAS cells (23 × 2 × 3 mm) with 63.5-μm Kapton tape windows. This operation was conducted in a nitrogen-filled glove bag. Immediately after their preparations, the samples were frozen in a liquid-nitrogen/*n*-hexane slurry to prevent autooxidation. X-ray absorption spectra were recorded at the Stanford Synchrotron Radiation Lightsource (SSRL) on beamline 9-3 (3 GeV, 100–50 mA) using a Si(220) double-crystal monochromator. Beamline 9-3 had an upstream collimating mirror and a downstream sagitally focusing mirror; both were rhodium-coated and also provided harmonic rejection. Data were collected as fluorescence spectra using a 30-element germanium array detector (39). For each sample, 10–21 scans were recorded from 6785 to 8257 eV. The energy was calibrated using an iron foil standard in which the first inflection point was assigned to an energy of 7111.2 eV (40). Data scans were averaged, background-subtracted, and normalized as described previously (41).

EXAFS Data Analysis—The model-fitting calculations were performed by means of the program *XFIT* (42). The values of the parameters that were varied to optimize the agreement between the observed and calculated EXAFS were the coordinates *x*, *y*, and *z* of all atoms in the model in relation to an arbitrary set of Cartesian axes, the Debye-Waller factors, σ^2, a scale factor, $S_0{}^2$, and E_0. The value of $S_0{}^2$ was initially restrained to be 0.9 with an estimated standard deviation (e.s.d.) 0.1 for O_2-αHb and 0.92 (e.s.d. 0.02) for O_2-αHb·AHSP (*i.e.* to typical values for low-spin O_2-myoglobin and O_2-leghemoglobin). Both the observed and calculated EXAFS were Fourier-filtered (42). The *k* windows used for the EXAFS analyses are shown in the figures. The goodness-of-fit parameter *R* was calculated as described by Ellis and Freeman (42). The model used in the *XFIT* analyses is that described previously (41). The sixth coordination site was a dioxygen molecule where the terminal oxygen was arbitrarily constrained to lie in the plane perpendicular to the heme and passing through the *meso*-Cs. The O^1-O^2 distance was restrained to be 1.22 Å (e.s.d. 0.01 Å), consistent with that reported by Jameson *et al.* (43). The constraints and restraints used for the bond lengths and bond angles in the porphyrin ring and the imidazole ligand and for the Debye-Waller factors were as described previously (41). Constraints and restraints and multiple-scattering (MS) paths used in the fitting calculations are given in supplemental Tables.

O_2/CO Binding Measurements—Rate constants for O_2 binding to and dissociation from ferrous αHb·AHSP complexes as well as rate constants for CO binding were measured using methods developed for relatively unstable Fe(II) O_2-Hb com-

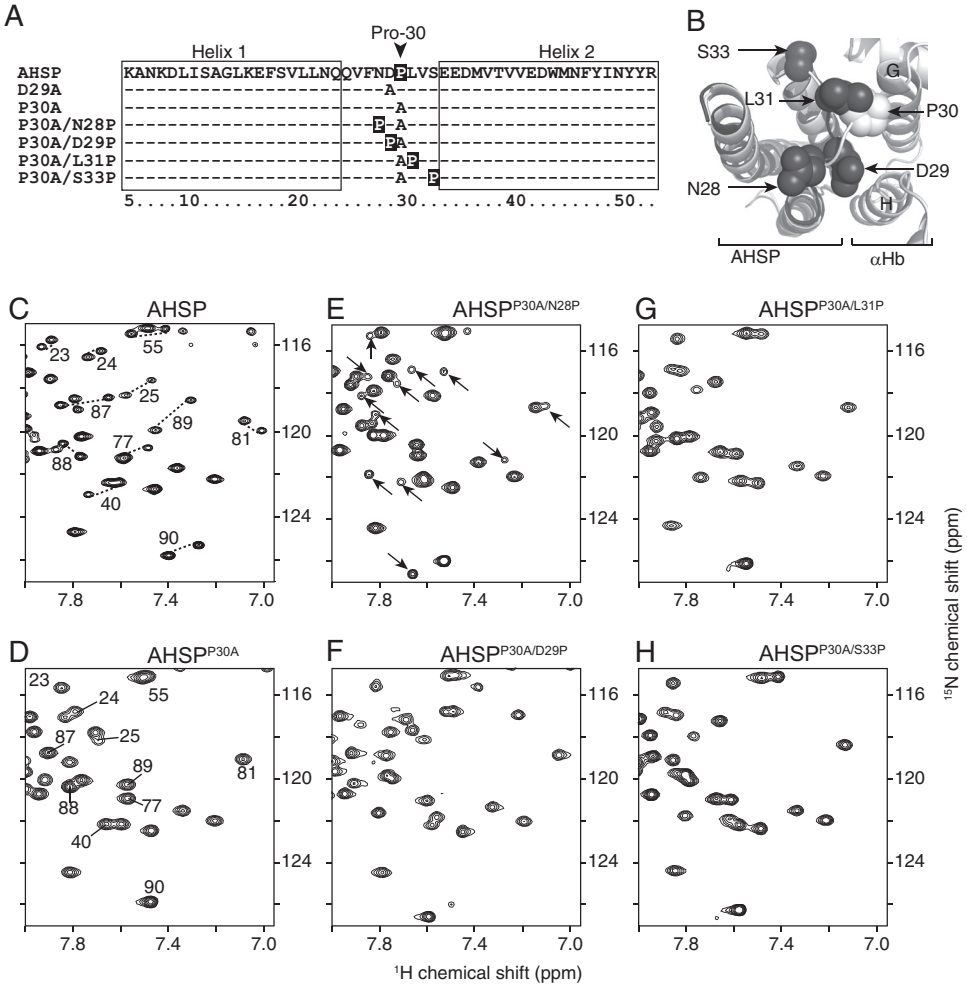

FIGURE 2. **Conformational exchange in AHSP is dependent on the position of proline residues in loop 1.** *A*, shown is the sequence of the first two α-helices and intervening loop 1 of wild-type human AHSP and AHSP mutants used in this study. Conserved positions relative to the wild-type sequence are marked with *dashes*. *B*, shown is the structure of the bis-histidyl αHb·AHSP interface (*white*, PDB 3IA3; the Pro-30 side chain is shown in *space-fill*) with the $AHSP^{P30A}$ structure overlaid (*black*, PDB 1Z8U). The positions of side chains mutated to proline in $AHSP^{P30A}$ are shown in *space-fill*. *C* and *D*, portions of the assigned ^{15}N-HSQC spectra of AHSP (800 μM) and $AHSP^{P30A}$ (900 μM). *E–H*, portions of the ^{15}N-HSQC spectra of $AHSP^{P30A/N28P}$ (400 μM), $AHSP^{P30A/D29P}$ (550 μM), $AHSP^{P30A/L31P}$ (900 μM), and $AHSP^{P30A/S33P}$ (530 μM) are shown. All ^{15}N-HSQC spectra were recorded at 15 °C in 20 mM sodium phosphate buffer, pH 6.9–7.0.

plexes as described by Birukou *et al.* (45). In these measurements, stable CO-αHb complexes are injected into laser photolysis cuvettes containing mixtures of buffers equilibrated with 1 atm O_2 or 1 atm CO. The mixtures in % were O_2:CO = 100:0, 75:25, 50:50, 25:75, and 0:100. The CO-αHb samples were photolysed with a 0.5-μs, 577-nm dye laser pulse. Absorbance time courses for O_2 and CO rebinding to deoxy-αHb were measured on μs time scales at 436 nm, and then time courses for replacement of the transiently bound O_2 by CO were measured on millisecond to seconds time scales at 424 nm (see Fig. 1 in Ref. 45). This method prevents significant autooxidation during the measurements of O_2 binding because the sample remains in the Fe(II)-CO form in between laser photolysis pulses. The dependence of the pseudo first order rates for the fast and slow phases on O_2 and CO were fitted globally to obtain values for the association rate constants for O_2 and CO binding to αHb, k'_{O2} and k'_{CO}, and the rate of O_2 dissociation, k_{O2}, as described in Birukou *et al.* (45). Our measurements were made using 100 mM potassium phosphate buffer, pH 7.0, at 20 °C. Similar kinetic measurements of O_2 and CO binding to native and recombinant wild-type Fe(II)-αHb·AHSP complexes were made by Vasseur-Godbillon *et al.* (28).

RESULTS

A Proline Residue Is Precisely Positioned in Loop 1 of AHSP to Promote Autooxidation of αHb—The Asp-29–Pro-30 peptide bond in loop 1 of AHSP undergoes *cis-trans* isomerization that is coupled with small changes in the packing of the three α-helices in AHSP (1, 46). Mutation of AHSP Pro-30 to a range of other residue types abolishes *cis-trans* peptidyl isomerization of AHSP and leads to a consistent 4-fold reduction in the rate of O_2-αHb autooxidation (11, 25). We previously proposed that *cis*-peptidyl Pro-30 makes physical contact with O_2-αHb that promotes autooxidation (25). However, it is possible that other changes in AHSP conformation related to *cis-trans* isomerization might explain the role of Pro-30 in αHb autooxidation. To investigate this possibility, we introduced proline mutations into $AHSP^{P30A}$ at position 28 ($AHSP^{P30A/N28P}$), 29 ($AHSP^{P30A/D29P}$), 31 ($AHSP^{P30A/L31P}$), or 33 ($AHSP^{P30A/S33P}$) as shown in Fig. 2*A*. We argued that proline residues in these positions might still allow

TABLE 1
αHb-interaction parameters for AHSP mutants

Protein	K_{autoox}, pH 7.0, 30 °C	Residues	N-H^N peaks[a]
	h^{-1}		
AHSP	0.59 ± 0.07	90[b]	121[b]
$AHSP^{P30A}$	0.14 ± 0.01	90	80
$AHSP^{D29A}$	0.53 ± 0.02	90	134[b]
$AHSP^{P30A/N28P}$	0.13 ± 0.02	90	113
$AHSP^{P30A/D29P}$	0.14 ± 0.03	90	84
$AHSP^{P30A/L31P}$	0.14 ± 0.05	90	85
$AHSP^{P30A/S33P}$	0.14 ± 0.03	90	81

[a] Spin systems with characteristic chemical shifts for Asn, Gln, Arg, and Trp side chains were excluded.
[b] The AHSP construct used comprises residues 1–90 with the C-terminal unstructured residues removed (1). Approximately 50% of residues gave rise to two sets of signals in triple resonance NMR spectra, corresponding to the *cis*/*trans* AHSP conformers. Differences in signal overlap in HSQCs results in a total of 121 resolved N-H^N peaks for WT AHSP and 134 resolved peaks for $AHSP^{D29A}$.

AHSP to undergo conformational exchange, but the proline side chains would presumably not preserve contacts with αHb that are made by the native Pro-30. The locations of the introduced proline mutations at the αHb·AHSP interface are shown in Fig. 2*B*. We did not mutate Val-32 because this side chain packs into the hydrophobic core between the AHSP helices.

The propensity of the mutant AHSP proteins to undergo *cis-trans* isomerization was assessed from ^{15}N-HSQC NMR spectra. A portion of the ^{15}N-HSQC spectrum of wild-type AHSP is shown in Fig. 2*C*, with peaks arising from N-H^N groups in the same residue in *cis*-prolyl and *trans*-prolyl conformers of AHSP labeled and joined by a *dashed line*. In the $AHSP^{P30A}$ spectrum, a single N-H^N peak was observed for each residue, consistent with a single AHSP conformer (Fig. 2*D* and Table 1) (1, 46). The spectrum of $AHSP^{P30A/N28P}$ contained an additional set of weaker HSQC signals compared with $AHSP^{P30A}$ (Fig. 2*E*, *arrows*, and Table 1) that was consistent with ~20% of molecules adopting an alternative conformation, most likely due to isomerization of the Phe-27–Pro-28 peptide bond. The ^{15}N-HSQC spectra of $AHSP^{P30A/D29P}$, $AHSP^{P30A/L31P}$, and $AHSP^{P30A/S33P}$ (Fig. 2, *F–H*) were all consistent with a single protein conformation, which indicated that prolines at positions 29, 31, and 33 do not result in measurable *cis*/*trans* isomerization. Chemical shift analyses were consistent with minor conformational changes in AHSP proximal to loop 1 and indicated that none of the mutations conferred gross structural changes (not shown). These results suggest that only *cis*-peptide bonds before Pro-30 or Pro-28 result in a significant amount of *cis*/*trans* isomerization.

The effect of AHSP proline mutations on αHb autooxidation is shown in Fig. 3. Autooxidation of O_2-αHb to bis-histidyl αHb was measured by changes in the visible absorption spectrum of αHb (Fig. 3, *A* and *B*). The absorbance time courses fit to single exponential expressions and yielded first-order rate constants for autooxidation (k_{autoox}; Fig. 3*C* and Table 1). $AHSP^{P30A}$ showed a 4-fold reduction in the value of the rate constant compared with that of wild-type AHSP, as previously described (11, 25). All introduced-proline mutants had the same low activity as the $AHSP^{P30A}$ (Fig. 3*C* and Table 1). A control mutation $AHSP^{D29A}$ had the same activity as wild-type AHSP. The results indicate that the positioning of Pro-30 in loop 1 is critical for function. In addition, the observation that free $AHSP^{P30A/N28P}$ showed *cis*/*trans* isomers in solution, yet conferred the same slowed rate of O_2-αHb autooxidation as $AHSP^{P30A}$, suggests that the propensity of free AHSP to undergo conformational changes does not in itself contribute to O_2-αHb·AHSP autooxidation activity. We have shown previously that stabilization of the *cis*-peptidyl Asp-29–Pro-30 AHSP conformation does correlate with increased autooxidation activity (25). Together the above data are consistent with the hypothesis that the effects of Pro-30 are mediated through direct contact between loop 1, containing the Pro-30 residue, and αHb.

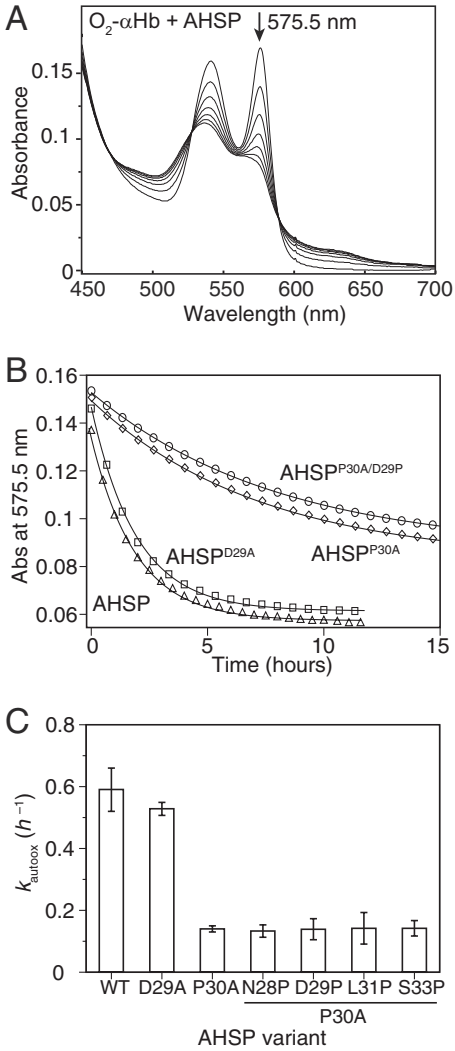

FIGURE 3. **The position of proline in AHSP loop 1 is important for function.** *A*, conversion of O_2-αHb·AHSP to bis-histidyl αHb·AHSP was monitored by a decrease in intensity of the absorption band at 575.5 nm. *B*, time courses for conversion to bis-histidyl αHb in the presence of AHSP or selected AHSP mutants are shown, with fits to an exponential function. *C*, rate constants for O_2-αHb conversion reactions using AHSP and AHSP mutants shown in Fig. 1*B* are shown (average ± S.D. for 3–9 repeat assays). Mutation of Pro-30 to Ala ($AHSP^{P30A}$) reduces the rate constants by a factor of 4. The control mutation ($AHSP^{D29A}$) had no significant effect. Introducing Pro at position 28, 29, 31, and 33 failed to rescue any activity.

Free Liganded αHb Monomer Adopts Native-like Secondary Structure—We next used NMR spectroscopy to probe for structural differences between αHb in the native Hb tetramer and free αHb in solution. The aim of these studies was to probe for structural changes in αHb that could explain the more rapid

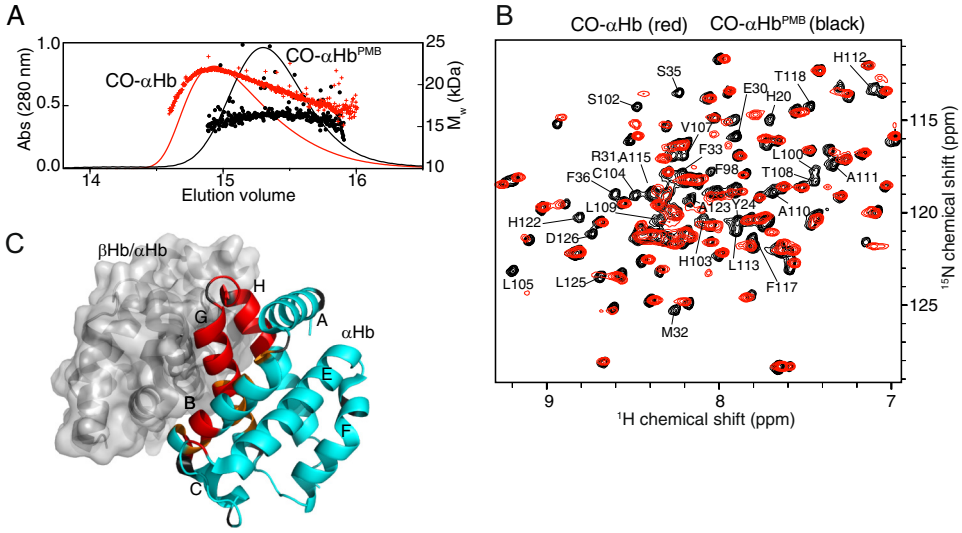

FIGURE 4. **Identification of the αHb homodimerization interface.** *A*, self-association of αHb was inhibited by treatment with pMB. SEC traces are shown for CO-αHb (*red*) or CO-αHb^{PMB} after reaction with a 4-fold molar excess of pMB (*black*). Molecular weight from light scattering measurements is plotted across each peak (*red*/*black symbols*). *B*, portions of the ^{15}N-HSQC for CO-αHb (*red*) and CO-αHb^{PMB} (*black*) were recorded at 15 °C in 20 mM sodium phosphate, pH 6.9. Assignments are shown for new peaks in the CO-αHb^{PMB} spectrum that are not present in the CO-αHb spectrum. *C*, shown are a ribbon (αHb) and surface (βHb) representation of the αHb/βHb dimer from CO-Hb (PDB 2DN3). Residues missing in the CO-αHb spectrum (*red*) or experiencing significant chemical shift difference between CO-αHb and CO-αHb^{PMB} (*orange*) map to the tight βHb-interaction face, which is, therefore, also identified as the αHb homodimerization face.

autooxidation observed *in vitro* and provide a suitable reference point for subsequent NMR studies of αHb·AHSP complexes. We found that sequential backbone assignments could not be obtained for residues 104–126 (corresponding to helices G and H), as also reported previously by Martineau and Craescu (47). The absence of NMR signals corresponding to these residues suggests that they might be in intermediate chemical exchange, perhaps as a result of αHb self-association.

In line with that possibility, we noted a marked decrease in SEC peak elution time with increasing αHb load concentration. This behavior is typical of protein self-association and is consistent with previous studies of αHb (48, 49). We reasoned that treatment of αHb with pMB, which covalently modifies Cys-104 of αHb and inhibits Hb chain homo (48) and hetero interactions (50), would allow more complete NMR data to be obtained. It has previously been shown that pMB treatment has no effect on the O_2 and CO binding parameters of isolated αHb (51). Light scattering was used to monitor the self-association status of CO-αHb before and after pMB treatment. We found that untreated CO-αHb eluted from SEC with a light scattering data profile characteristic of reversible self-association, with a marked increase in M_w toward the center (*i.e.* the highest concentration) of the elution peak (Fig. 4*A*, each M_w measurement is indicated with a *red* +). In contrast, pMB treated CO-αHb (CO-αHb^{PMB}) eluted with a constant M_w of 16.7 ± 1.3 across the peak (Fig. 4*A*, *black dots*), indicating that CO-αHb^{PMB} is predominantly monomeric (formula weight of 16,053).

The ^{15}N-HSQC spectrum of CO-αHb^{PMB} (Fig. 4*B*, *black*) contained numerous additional peaks (labeled) that were not present in the untreated CO-αHb spectrum (Fig. 4*B*, *red*) and sequential backbone assignments could now be obtained for 130/134 non-proline residues of CO-αHb^{PMB}. Comparison of the CO-αHb^{PMB} and CO-αHb backbone chemical shifts indicated that only the modified Cys-104 and immediately surrounding residues were strongly influenced (not shown), confirming that pMB modification does not substantially alter the tertiary structure of αHb, consistent with functional measures of O_2 and CO binding (51). The αHb self-association interface is clearly identified by the NMR data (Fig. 4*C*, *red*/*orange*) and is the same face that interacts with βHb (Fig. 4*C*, *surface*) to form the $\alpha Hb_1\beta Hb_1$ heterodimer.

To obtain information about the secondary structure of monomeric CO-αHb^{PMB}, we used TALOS+ (52) to derive ϕ and ψ backbone angle predictions from NMR chemical shift data. Seven helical secondary structure elements could be clearly identified corresponding to the A-C and E-H helices (Fig. 5). The angles derived by TALOS+ were very similar to angles determined from crystal structures of native CO-Hb (PDB 2DN3) (53), with correlation coefficients of 0.82 (ϕ) and 0.87 (ψ) over 127 residues. One difference was that TALOS+ consistently assigned the C helix region as α-helix rather than the 3_{10}-helix that is identified by the program DSSP (54) based on crystal structure coordinates (PDB 2DN3).

To obtain information about the heme pocket, we assigned His side chain resonances for CO-αHb^{PMB} (Fig. 6 and Table 2). His-58 and His-87 side chain resonances displayed large upfield deviations from random coil chemical shifts consistent with positions above or below the plane of the heme ring. The chemical shifts were very similar to values previously obtained for CO-αHb at pH 5.3–5.7, 36 °C, (55, 56), and the αHb subunit of intact CO-Hb at pH 6.9, 29 °C (30, 57), strongly supporting the conclusion that free αHb adopts a heme pocket structure similar to that in Hb tetramers, with the heme iron bound through $N^{\epsilon 2}$ of His-87. In summary, preparation of monomeric αHb through treatment with pMB allowed us to obtain backbone and His side chain chemical shift data suitable for comparative NMR studies with αHb·AHSP complexes.

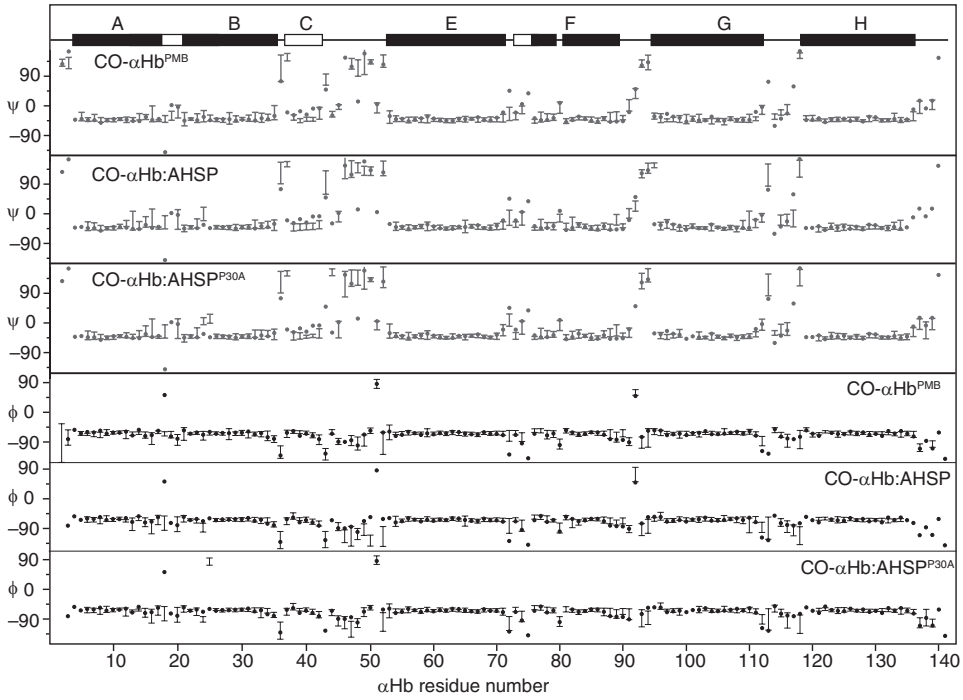

FIGURE 5. **NMR chemical shift-derived ψ angles for αHb in the absence and presence of AHSP.** Backbone ψ and ϕ angle predictions were calculated from H^N, ^{15}N, $^{13}C^{\alpha}$, and $^{13}C^{\beta}$ chemical shifts using the program TALOS+ (52). Predictions for CO-αHb^{PMB}, CO-αHb·AHSP, and CO-αHb·AHSP^{P30A} are displayed as *bars* with a height ±1 S.D. The ψ and ϕ angles from the αHb subunit of a CO-HbA crystal structure (PDB 2DN3) are superimposed (*filled circles*) with α-helix (*black bars*) and 3_{10} helix (*white bars*) secondary structure elements as assigned by DSSP (54).

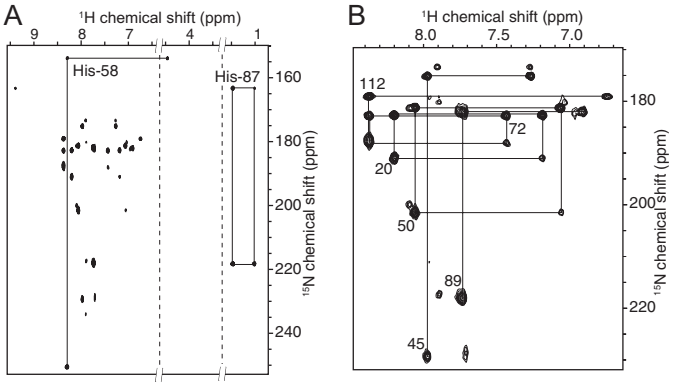

FIGURE 6. **Histidine region of the ^{15}N-HSQC spectrum of CO-αHb^{PMB}.** *A*, shown is a portion of ^{15}N-HSQC spectrum of CO-αHb^{PMB} (0.8 mM) in 20 mM sodium phosphate, pH 7.0, at 15 °C. The heme pocket His-58 and His-87 spin systems contain highly shifted resonances (linked by *solid lines*). Note that axes are discontinuous to remove large empty regions of the spectrum. *B*, shown is the central region of the spectrum shown in *A* with peaks assigned to surface histidine side chains.

TABLE 2

NMR resonances of His side chains for CO-αHb^{PMB} and CO-αHb·AHSP

Resonances for CO-αHb^{PMB} in 10 mM sodium phosphate, pH 7.0, at 288 K and CO-αHb·AHSP in 10 mM sodium phosphate, pH 7.0, at 298 K.

His residue	$N^{\delta 1}$	$N^{\epsilon 2}$	$H^{\delta 2}$	$H^{\epsilon 1}$	$H^{\delta 1}$
20	191.0	182.7	7.20	8.21	
45	229.0	175.1	7.27	7.99	
50	201.4	181.2	7.06	8.07	
58	250.6	153.8	4.47	8.30	
72	188.1	182.8	7.44	8.38	
87	163.3	218.2	1.02	1.47	9.40
89	218.0	182.0	6.92	7.74	
112	187.3	179.1	6.76	8.38	
58 (with AHSP)	250.1	153.8	4.48	8.05	
87 (with AHSP)	163.2	218.6	1.10	1.43	9.31

CO-αHb Retains Near-native Secondary Structure and Heme Ligation in Complex with AHSP—To understand how AHSP promotes autooxidation of αHb, we examined chemical shift differences between free CO-αHb^{PMB} and the CO-αHb·AHSP complex. Widespread changes in the ^{15}N-HSQC of CO-αHb were observed upon binding of AHSP (Fig. 7*A*) despite the complex remaining in the CO-liganded form, as confirmed by UV-visible spectroscopy (not shown). A plot of backbone chemical shift differences between CO-αHb^{PMB} and CO-αHb·AHSP reveals that the B-C corner and the F, G, and H helices of αHb are most affected (Fig. 7*B*).

The B-C corner, helix G, and helix H comprise the AHSP binding face of αHb (1, 2, 25), and chemical shift changes are expected here as a result of the interface forming (Fig. 7*B*, *gray background shading*). In contrast, chemical shift changes in helix F cannot be explained by proximity to the AHSP surface, which implies that they arise from an induced structural change in αHb. However, NMR signals arising from the F helix region had similar line widths to signals from other regions of the αHb subunit, and TALOS+ derived ϕ and ψ angles indicated that the F helix region remains well ordered with similar secondary structure in the absence and presence of AHSP (Fig. 5).

His-87 side chain resonances remained strongly shifted in the complex with AHSP (Fig. 8*A*, *red*), with similar chemical shift values to the free CO-αHb^{PMB} form (Fig. 8*A*, *black*). This provides strong evidence that His-87 remains the heme-ligating residue in CO-αHb·AHSP. In summary, AHSP binding to CO-αHb results in small but significant conformational changes in helix F even though the α-helical character and heme binding function are retained. As such, these findings contrast with a previous x-ray crystallographic study in which we reported that O_2-αHb·AHSP^{P30A} has a highly unusual heme

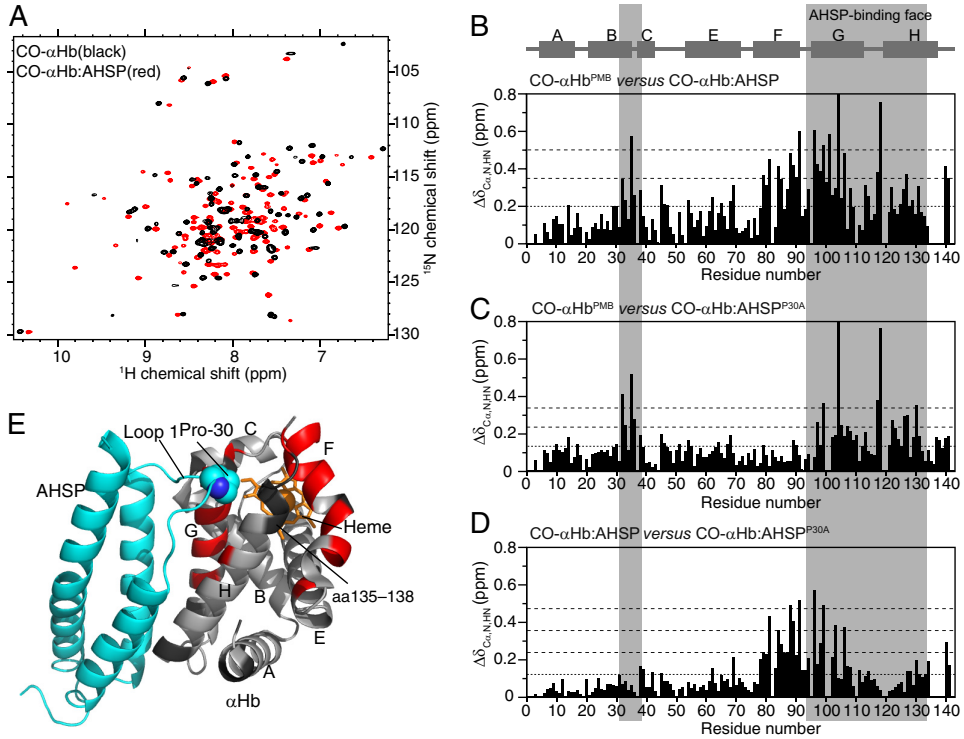

FIGURE 7. **AHSP binding perturbs helix F of CO-αHb^{PMB}.** *A*, shown are ^{15}N-HSQC spectra of CO-αHb and CO-αHb·AHSP recorded at 298 K in 20 mM sodium phosphate, pH 7.0. *B*, shown are combined, weighted, chemical shift differences ($\Delta\delta_{N,HN,C\alpha}$) between CO-αHb^{PMB} (15 °C) and CO-αHb·AHSP (25 °C). *C*, shown are chemical shift differences between CO-αHb^{PMB} (15 °C) and CO-αHb·AHSP^{P30A} (25 °C). *D*, shown are αHb chemical shift differences between the CO-αHb·AHSP and CO-αHb·AHSP^{P30A} complexes (both at 25 °C). *Horizontal dotted* and *dashed lines* indicate the average Δδ and increments of 1 S.D., respectively. *E*, shown is a molecular model of the O_2-αHb·AHSP complex generated by substituting O_2-αHb (PDB 2DN1) for the bis-histidyl αHb subunit in the bis-histidyl αHb·AHSP crystal structure (PDB 3IA3). Residues in αHb experiencing a chemical shift difference ($\Delta\delta_{N,HN,C\alpha}$) >0.2 ppm between the AHSP and AHSP^{P30A} complexes are colored *red* (residues missing assignments in one or both complexes are *black*).

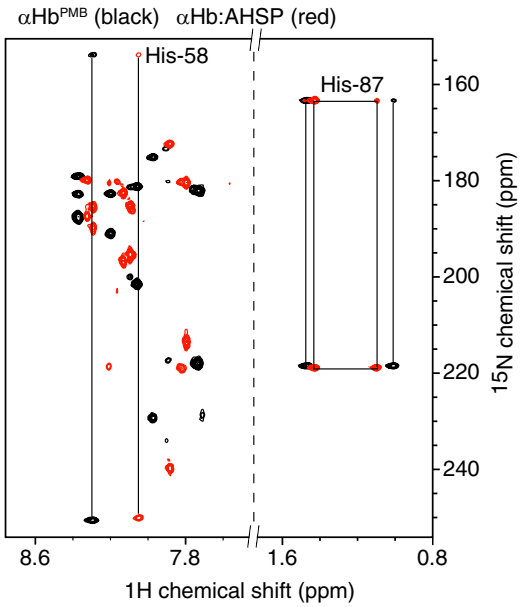

FIGURE 8. **His-87 is the heme ligand in O_2-αHb·AHSP.** Overlay of portion of the ^{15}N-HSQCs of CO-αHb^{PMB} (20 mM sodium phosphate, pH 7.0, 15 °C; *black*) and CO-αHb·AHSP (20 mM sodium phosphate, pH 7.0, 25 °C; *red*) show that the His-58 and His-87 side chains experience only minor chemical shift perturbations upon AHSP binding.

site geometry wherein the F helix is disordered, and heme is coordinated by His-58 in helix E (1). It is possible that the unusual crystal structure is characteristic of the O_2- and not the CO-αHb·AHSP complex but, as described below, that now seems unlikely at least for the O_2-αHb·AHSP complex in solution.

AHSP Pro-30 Perturbs the Proximal Heme Pocket of αHb—Because mutation of AHSP Pro-30 to Ala or other residue types leads to a 4-fold decrease in the rate of O_2-αHb·AHSP autooxidation, we reasoned that CO-αHb·AHSP and CO-αHb·AHSP^{P30A} complexes would display structural differences that give insight into the mechanism underlying AHSP-mediated αHb autooxidation. We, therefore, obtained backbone resonance assignments for CO-αHb in complex with AHSP^{P30A} using standard triple resonance methods. Compared with wild-type AHSP, the AHSP^{P30A} mutant induced more limited perturbations of CO-αHb (Fig. 7*C*). A direct comparison of CO-αHb chemical shifts in the CO-αHb·AHSP and CO-αHb·AHSP^{P30A} complexes shows that the wild-type AHSP causes significantly larger chemical shift perturbations to the N-terminal fragment of αHb helix G and the whole of helix F (Fig. 7*D*), which suggests that AHSP Pro-30 makes contacts that are transmitted through the αHb structure and lead to perturbations of helix F.

Interestingly, we could not obtain backbone assignments for residues 135–138 of CO-αHb in complex with wild-type AHSP, and signals for these residues appeared to be absent from the NMR spectra. In NMR spectra of CO-αHb·AHSP^{P30A}, residues 135–138 were assigned and predicted as the regular α-helix by TALOS+ (Fig. 5). Residues 135–138 of native αHb are in a region of helix H that contacts helix F (Fig. 7*E*), which suggests that loss of NMR signals could reflect a destabilization of helix

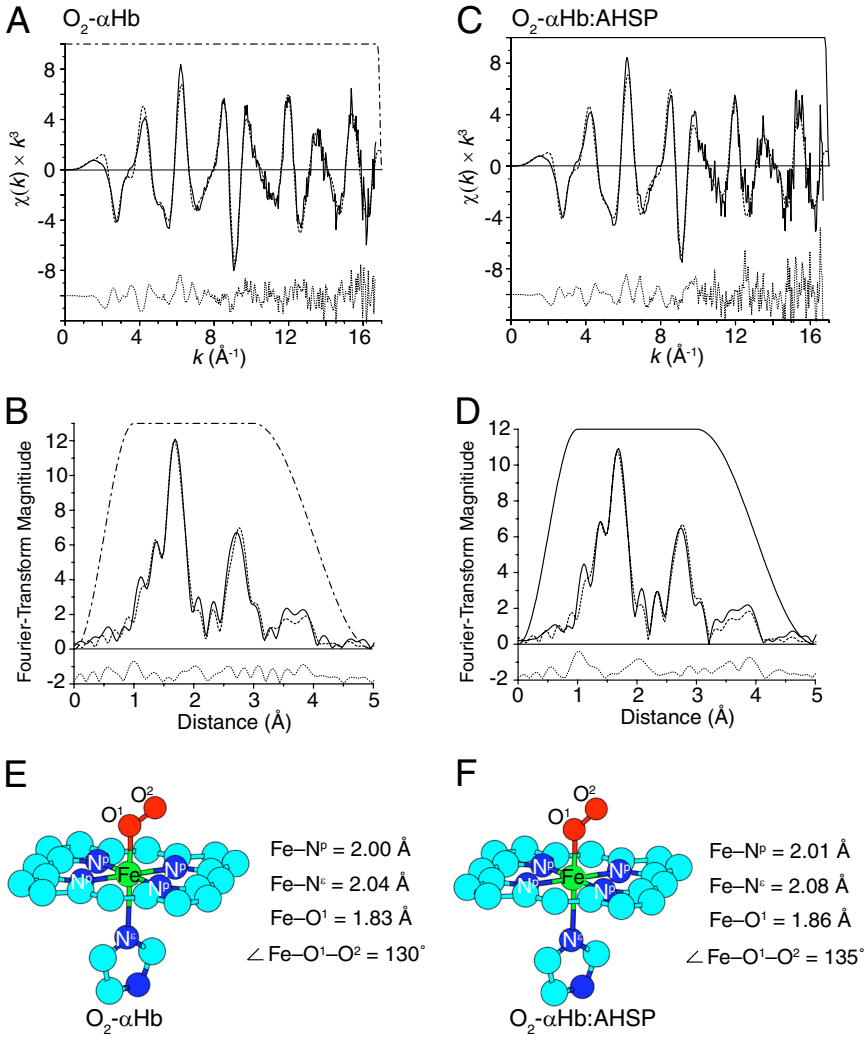

FIGURE 9. **EXAFS analyses of the heme sites of O_2-αHb and O_2-αHb·AHSP.** Shown are EXAFS (*A*) and Fourier-transform amplitude (*B*) of EXAFS of O_2-αHb. Shown are EXAFS (*C*) and Fourier-transform amplitude (*D*) of EXAFS of O_2-αHb·AHSP. Shown are the observed data (*solid line*), data calculated from the best fit to the model (*dashed line*), residual data (*dotted line*), and window used in the Fourier filter (*dot-dash*). Molecular structures and Fe-ligand bond lengths and Fe-O–O bond angle for O_2-αHb (*E*) and O_2-αHb·AHSP (*F*) were obtained from EXAFS data.

H in αHb·AHSP related to changes in structure of the F helix. Overall the results here indicate that AHSP Pro-30 makes contacts that perturb helices F, G, and H of αHb, which together constitute the proximal heme pocket of αHb (Fig. 7*E*).

Comparison of the Iron-Ligand Structures in O_2-αHb and O_2-αHb·AHSP—NMR spectroscopic data indicated that His-87 is retained as the iron binding His residue in CO-αHb·AHSP, but these data do not provide detailed information about the exact geometries of the axial iron ligands. In addition, we could not determine NMR structures for the O_2-αHb·AHSP complexes due to autooxidation during NMR data collection. To probe the electronic structure and coordination environment around the heme iron more directly, we acquired x-ray absorption spectra at the iron K-edge for the physiologically more relevant O_2-αHb and O_2-αHb·AHSP complexes. Spectra were recorded at 10 K to minimize photo-damage and increase the importance of multiple-scattering contributions to the EXAFS (58, 59). Samples were prepared in buffer containing 0.88 M sucrose, which allowed the formation of a homogeneous glass upon freezing (59). This procedure permitted measurements on the unstable O_2-αHb·AHSP complex to be performed over extended time periods without conversion to the bis-histidyl ferric αHb form. The x-ray absorption near edge structure (XANES) spectra of O_2-αHb and O_2-αHb·AHSP (not shown) show no irradiation damage, and the similarity to spectra of the low-spin Fe(III) proteins metleghemoglobin, oxymyoglobin, and oxyleghemoglobin (60) suggest that all have a low-spin Fe(III) center, which is consistent with an $Fe(III)^{+}$-O_2^{-} species (61). This classification is also supported by the diagnostic oxidation- and spin-state resonance Raman marker bands (1, 62). The slightly lower edge energy of O_2-αHb·AHSP compared with free O_2-αHb suggests a lengthening of the Fe-O_2 bond in the AHSP complex.

EXAFS data obtained from O_2-αHb and O_2-αHb·AHSP were fitted to models for the iron sites using restrained and constrained multiple-scattering models (58, 63–65). The observed and calculated EXAFS and the corresponding Fourier transforms are shown for O_2-αHb and O_2-αHb·AHSP in Fig. 9, *A–D*, and the derived molecular structures for O_2-αHb and O_2-αHb·AHSP are shown in Fig. 9, *E* and *F*, respectively. The

TABLE 3
A comparison of Fe-ligand geometry from EXAFS and X-ray crystallographic analyses

Species	Method	Fe-Ligand distances				Fe-O-O angle (°)	Debye-Waller factors, σ^2				Other fit parameters		
		N^p	N^ϵ	O^1	O^1-O^2		N^p	N^ϵ	O^1	O^2	E_0	S_0^2	R
		Å					*Å*				*eV*		*%*
O_2-αHb	Crystal[a]	2.02 (8)	2.07 (8)	1.82 (8)	1.23 (8)	124							
	MS[b]	2.00 (2)	2.04 (2)	1.83 (2)	1.21 (2)	130 (3)	0.002	0.001	0.003	0.004	7125.1 (2)	0.92 (2)	15.9
O_2-αHb·AHSP	Crystal[c]	2.0 (5)	2.1 (5)	2.7 (5)	1.3 (5)	143							
	MS[d]	2.01 (2)	2.08 (2)	1.86 (2)	1.22 (2)	135 (3)	0.001	0.002	0.002	0.008	7125.4 (3)	0.915 (3)[e]	16.8
	MS[f]	2.03[f]	2.12[f]	2.74[f]	1.25[f]	143[f]	0.002	0.059	0.079	0.080	7131.2	0.932	32.5

[a] PDB 2DN1 data at 1.25 Å resolution. Bond length errors are Cruickshank diffraction-data precision indicator (DPI) as calculated by REFMAC multiplied by $2^{1/2}$ to convert from average coordinate error to average bond length error.
[b] This work; 12-scan average. Error estimates in parentheses are calculated as described under "Comparison of the Iron-Ligand Structures."
[c] PDB 1Y01 data at 2.8 Å resolution. Bond length errors are $2^{1/2} \times$ DPI based on R_{free} factor.
[d] This work; 21-scan average. Error estimates in parentheses are calculated as described under "Comparison of the Iron-Ligand Structures."
[e] Restraint on S_0^2 was tightened to be 0.92(2) Å^2; *i.e.*, similar to O_2-αHb.
[f] Iron−ligand bond lengths and Fe-O-O bond angle were constrained to be those in the O_2-αHb·AHSP^{A30} structure (PDB 1Y01).

bond length/angle and other fitted parameters obtained are listed in Table 3.

The errors in the iron-ligand bond lengths determined by EXAFS were estimated as the r.m.s. of contributions from both random and systematic errors. The random (statistical) errors due to noise in the data were estimated by Monte-Carlo calculations (42), and the systematic errors were assigned a conservative consensus value, 0.02 Å (44). For O_2-αHb, the calculated statistical errors were 0.002 Å for Fe-N^p, 0.008 Å for Fe-N^ϵ, and 0.005 Å for Fe-O_2. For O_2-αHb·AHSP, Monte-Carlo calculations yielded r.m.s. errors of 0.003 Å for Fe-N^p, 0.012 Å for Fe-N^ϵ, and 0.006 Å for Fe-O_2. These statistical errors were combined with the maximum systematic error to obtain the estimated maximum r.m.s. errors in the reported bond lengths (Table 3). Monte-Carlo calculations yielded an r.m.s. error of 1.7° and 2.3° for the Fe-O-O bond angle in O_2-αHb and O_2-αHb·AHSP, respectively. These errors were combined with the respective r.m.s. errors of 2.1° and 3.2°, resulting from varying the O-O distance by ±0.03 Å (Table 4) to give respective estimated maximum r.m.s. errors of 2.7° and 3.9° for O_2-αHb and O_2-αHb·AHSP. Therefore, the error in this bond angle estimated by two independent methods is ~3–4°. The resulting Fe-O-O angles determined from restraining the starting angle between 115° and 175° and allowing the fit to go to convergence then removing the restraint were 130° (for 6 minima and 143° for 1 minimum; the latter was a local minimum with a higher R value and a low S_o^2 value for a heme protein) in O_2-αHb (Table 5) and 135° (for 6 minima and 101° for 1 minimum) in O_2-αHb·AHSP (Table 6). The fit obtained for the Fe-O-O bond angle of 101°, when the angle was initially restrained to be 115° and then this restraint was removed and the fit allowed to go to convergence, is likely to be a false minimum. This is because it is not chemically reasonable and is not consistent with the similarity in the shape of the XANES of O_2-αHb and O_2-αHb·AHSP (not shown), as XANES is sensitive to bond angles. These analyses show that the bond lengths are independent of all of these changes in starting models and constraints/restraints, and the bond angles relax to the non-constrained values shown in Table 3. These detailed analyses of parameter space provide confidence that the EXAFS fits are robust and are not trapped in false minima. Similarly, varying the tilt or rotation of the proximal imidazole did not significantly alter the fitted bond length parameters (not shown).

Overall the iron-site geometry of O_2-αHb and O_2-αHb·AHSP is similar to that derived from high resolution (1.25 Å) crystal structures of O_2-HbA (53). However, the Fe-N_ϵ and Fe-O bond lengths were shorter in O_2-αHb than in O_2-αHb·AHSP (2.04 *cf.* 2.08 Å and 1.83 *cf.* 1.86 Å). Although these differences are within the conservative estimates of accuracy given in Table 3 (0.02 Å), the systematic error contributions are expected to be the same for both proteins and, hence, the errors obtained from Monte Carlo calculations are a better indication of the relative errors. For the Fe-O_2 bond these errors were 0.005 and 0.006 Å in O_2-αHb and O_2-αHb·AHSP, respectively, indicating that the 0.03 Å lengthening of Fe-O_2 in O_2-αHb·AHSP is significant. It should be emphasized that the Fe-O_2 bonds are substantially shorter than those of the other heme-ligand bonds, which is why the precision is so high. This is due to the rapid increase in the importance of single and multiple-scattering contributions as the bond length decreases.

The O_2-αHb·AHSP data were also fitted to a model where the iron-ligand bond lengths and Fe-O-O bond angle were constrained to be that in the O_2-αHb·AHSP^{P30A} structure (1), and E_0, S_0^2, and the Debye-Waller factors were fitted (Table 3, *bottom row*). The resulting temperature factors were unacceptably high (0.059 Å^2 for the proximal imidazole N^ϵ, 0.079 Å^2 for O^1, and 0.080 Å^2 for O^2) with an R value of 32.5%. Clearly, this model does not fit the solution structure.

The ability of this methodology to determine precise bond length and angle information on axial ligands has been established in studies of porphyrin model complexes and by the determination of precise bonding parameters in the heme environments of met- and deoxymyoglobin (41, 66) before the publication of the high resolution protein crystallographic structures (67, 68). Even taking the small differences between O_2-αHb·AHSP and O_2-αHb into account, it is clear that the initial solution complex of O_2-αHb·AHSP has a "normal" coordination geometry similar to that in free O_2-αHb chains.

AHSP Reduces Reactivity of αHb with O_2 and CO—In 2006, Vasseur-Godbillon *et al.* (28) reported that AHSP binding reduces the O_2 and CO affinities of αHb roughly 3–5-fold. We repeated these ligand binding experiments with wild type and two Pro-30 mutants of AHSP. Table 7 presents a summary of the rate constants for O_2 and CO association (k'_{O2} and k'_{CO}) to, and O_2 dissociation (k_{O2}) from, αHb in the presence and

TABLE 4

Effect of varying the O-O bond distance restraint on the Fe-O-O angle in human O_2-αHb and O_2-αHb·AHSP

The quantities enclosed by the brackets ({}) are the values of σ_{res} used by XFIT, which is analogous to e.s.d.

Species	Restraint on O-O bond {σ_{res}}	Fe-Ligand distances				Fe-O-O angle	Debye-Waller Factors, σ^2			S_0^2	R
		N^p	N^ϵ	O^1	O^2		N^p	N^ϵ	O^1		
	Å	Å				°	Å^2				%
O_2-αHb	1.19 {0.01}	2.00	2.04	1.83	1.18	131.4	0.001	0.001	0.003	0.920	14.8
	1.25 {0.01}	2.00	2.04	1.83	1.25	133.5	0.001	0.001	0.003	0.906	15.4
	1.22 {0.03}	2.00	2.04	1.83	1.21	130	0.002	0.001	0.003	0.92	15.9
O_2-αHb·AHSP	1.19 {0.01}	2.00	2.08	1.86	1.19	137.6	0.001	0.002	0.002	0.916	16.8
	1.25 {0.01}	2.01	2.08	1.86	1.25	134.0	0.001	0.002	0.002	0.915	16.8
	1.22 {0.03}	2.01	2.08	1.86	1.22	135	0.001	0.002	0.002	0.915	16.8

TABLE 5

Effect of restraining the Fe-O-O bond angle in human O_2-αHb on the MS XAFS analysis

The quantities enclosed by the brackets ({}) are the values of σ_{res} used by XFIT, which is analogous to e.s.d.

Restraint on Fe-O-O bond angle {σ_{res}}	Fe-Ligand distances				Fe-O-O angle (°)	Debye-Waller factors, σ^2				S_0^2	R
	N^p	N^ϵ	O^1	O^2		N^p	N^ϵ	O^1	O^2		
	Å					Å					%
115° {1°}	2.00	2.05	1.83	1.22	115.0	0.001	0.001	0.003	0.080	0.893	15.9
125° {1°}	2.00	2.04	1.83	1.22	126.6	0.001	0.001	0.003	0.004	0.902	15.2
135° {1°}	2.00	2.05	1.83	1.21	134.9	0.001	0.001	0.003	0.009	0.909	15.3
145° {1°}	2.00	2.05	1.83	1.22	144.6	0.001	0.001	0.003	0.004	0.886	15.6
155° {1°}	2.00	2.05	1.83	1.22	155.0	0.001	0.001	0.003	0.080	0.895	15.8
165° {1°}	2.00	2.05	1.83	1.22	165.0	0.001	0.001	0.003	0.080	0.894	15.9
175° {1°}	2.00	2.05	1.83	1.22	175.0	0.001	0.001	0.003	0.080	0.894	15.9
No constraint	2.00	2.05	1.83	1.21	129	0.001	0.001	0.003	0.004	0.919	14.1
115°[b]	2.00	2.04	1.83	1.21	129.7	0.002	0.001	0.003	0.004	0.922	15.0
125°[b]	2.00	2.04	1.83	1.21	129.7	0.002	0.001	0.003	0.004	0.922	15.0
135°[b]	2.00	2.04	1.83	1.21	129.7	0.002	0.001	0.003	0.004	0.922	15.0
145°[b]	2.00	2.06	1.84	1.22	143.4	0.001	0.001	0.003	0.004	0.884	15.6
155°[b]	2.00	2.04	1.83	1.21	129.7	0.002	0.001	0.003	0.004	0.922	15.0
165°[b]	2.00	2.04	1.83	1.21	129.7	0.002	0.001	0.003	0.004	0.922	15.0
175°[b]	2.00	2.04	1.83	1.21	129.7	0.002	0.001	0.003	0.004	0.922	15.0

[a] The original fit where Fe-O-O is unrestrained is included for comparison.
[b] Fits were performed in which the Fe-O-O angles restrained the starting angle between 115° and 175° and then allowed the fit to go to convergence, then removing the restraint.

TABLE 6

Effect of restraining the Fe-O-O bond angle in human O_2-αHb·AHSP on the MS XAFS analysis

The quantities enclosed by the brackets ({}) are the values of σ_{res} used by XFIT, which is analogous to e.s.d.

Restraint on Fe-O-O Bond angle {σ_{res}}	Fe-Ligand distances				Fe-O-O angle	Debye-Waller factors, σ^2				S_0^2	R
	N^p	N^ϵ	O^1	O^2		N^p	N^ϵ	O^1	O^2		
	Å				°	Å^2					%
115° {1°}	2.01	2.08	1.86	1.22	115.0	0.001	0.003	0.002	0.080	0.914	17.4
125° {1°}	2.01	2.08	1.86	1.23	126.7	0.001	0.002	0.002	0.010	0.915	17.3
135° {1°}	2.01	2.08	1.86	1.22	135.1	0.001	0.002	0.002	0.008	0.915	16.8
145° {1°}	2.01	2.07	1.86	1.22	144.6	0.001	0.003	0.002	0.029	0.914	17.3
155° {1°}	2.01	2.08	1.86	1.22	155.0	0.001	0.003	0.002	0.080	0.914	17.4
165° {1°}	2.01	2.08	1.86	1.22	165.0	0.001	0.003	0.002	0.080	0.914	17.4
175° {1°}	2.01	2.08	1.86	1.22	175.0	0.001	0.003	0.002	0.080	0.914	17.4
No constraint	2.01	2.08	1.86	1.22	135	0.001	0.002	0.002	0.008	0.915	16.8
115°[b]	2.01	2.07	1.86	1.22	101	0.001	0.004	0.002	0.004	0.914	14.7
125°[b]	2.01	2.08	1.86	1.22	135.4	0.001	0.002	0.002	0.008	0.915	16.8
135°[b]	2.01	2.08	1.86	1.22	135.4	0.001	0.002	0.002	0.008	0.915	16.8
145°[b]	2.01	2.08	1.86	1.22	135.4	0.001	0.002	0.002	0.008	0.915	16.8
155°[b]	2.01	2.08	1.86	1.22	135.4	0.001	0.002	0.002	0.008	0.915	16.8
165°[b]	2.01	2.08	1.86	1.22	135.4	0.001	0.002	0.002	0.008	0.915	16.8
175°[b]	2.01	2.08	1.86	1.22	135.4	0.001	0.002	0.002	0.008	0.915	16.8

[a] The original fit where Fe-O-O is unrestrained is included for comparison.
[b] Fe-O-O angles were initially restrained between 115° and 175° and the fit allowed to go to convergence, then the restrain was removed and the fit allowed to go to convergence.

absence of AHSP variants. The ratio of k'_{O2}/k_{O2} provides the O_2 association equilibrium or affinity constant (K_{O2}). As reported by Vasseur-Godbillon *et al.* (28), AHSP binding to O_2-αHb causes a small decrease in the rate of O_2 binding and a larger 3–4-fold increase in the rate of O_2 dissociation. The net result is an ~4-fold decrease in O_2 affinity (Table 7). These results support the XAFS data and provide direct evidence that AHSP binding leads to weakening of the Fe-O_2 bond, which in turn leads to a significant increase in the susceptibility of O_2-αHb to autooxidation.

AHSP binding to αHb also slows the rate of bimolecular CO binding by a factor of ~3–4-fold, as also reported previously by Vasseur-Godbillon *et al.* (28) (Table 7). CO binding is limited primarily by the rate of internal bond formation and, therefore, provides a sensitive measure of iron reactivity that is primarily determined by interactions between the heme iron and the

TABLE 7
AHSP·αHb ligand binding kinetic parameters at pH 7, 20 °C

Protein	k'_{O2}	k_{O2}	k'_{CO}	K_A,O_2
	$\mu M^{-1}\ s^{-1}$	s^{-1}	$\mu M^{-1}\ s^{-1}$	
αHb	37 ± 9 (40 ± 2)[a] (50)[b]	29 ± 7 (22 ± 6)[a] (40)[b]	5.3 ± 0.3 (5.2 ± 0.5)[a] (6)[b]	1.3 ± 0.5 (1.8 ± 0.5)[a] (1.2)[b]
AHSP·αHb[c]	23 (35)[b]	73 (130)[b]	1.4 (2)[b]	0.30 (0.35)[b]
$AHSP^{P30A}$·αHb	35	47	2.2	0.7
$AHSP^{P30W}$·αHb	28	25	3.8	1.1

[a] Rate parameters were taken from Birukou *et al.* (45).
[b] These values were measured at pH 7.0, 25 °C by Vasseur-Godbillon *et al.* (28).
[c] The values of the kinetic parameters for AHSP·αHb represent the average of two independent determinations.

proximal histidine. The ~4-fold decrease in k'_{CO} and O_2 affinity are consistent with conformational strain introduced on the proximal side of the heme pocket of αHb·AHSP due to interactions with AHSP Pro-30. This interpretation is strongly supported by the effects of Pro-30 mutations on ligand binding. As shown in Table 7, $AHSP^{P30A}$ and $AHSP^{P30W}$ mutations diminish the effects of AHSP binding on both O_2 affinity and the rate of CO association, and in the case of $AHSP^{P30W}$, the observed ligand binding parameters are similar to those of free αHb. Thus, all our structural, spectroscopic, and functional data suggest that structural changes in the proximal heme pocket are induced by AHSP Pro-30, causing a weakening of the Fe-O_2 bond and an increase in the rate of autooxidation.

DISCUSSION

AHSP promotes autooxidation of O_2-αHb to prevent it from reacting with H_2O_2 under conditions of oxidative stress. The resultant bis-histidyl heme does not react with H_2O_2 and, therefore, cannot generate reactive ferryl species and protein radicals (2, 20). The bis-histidyl αHb·AHSP structure has been well characterized by x-ray crystallographic and spectroscopic methods (1, 2, 25–27), but the formation of this structure from O_2-αHb has been less well understood. The data presented here provide key insights as to how AHSP facilitates formation of the bis-histidyl state by making specific interactions at the αHb·AHSP interface and fit a model, explained below, in which αHb·AHSP complexes can adopt one of two well ordered conformations that are intermediates in Hb assembly and achieve αHb detoxification (Fig. 10).

Structure of αHb—By reacting pMB with Cys-104 and blocking αHb self-association, we obtained chemical shift-derived backbone dihedral angles and chemical shift analysis of His side chains, which together show that the conformation of free αHb is very similar to its structure in the native Hb tetramer. This conclusion is consistent with previous findings that heme pocket structure is well preserved in isolated subunits, based on far-UV (69, 70) and near-UV CD (69–72) and homonuclear NMR studies of ferrous and ferric αHb (47, 55, 56, 73, 74). None of these data provide any hints as to why free αHb is more prone to oxidation and subsequent rapid loss of the heme moiety and aggregation. Similar observations have been made in other systems. For example, the monomeric point mutants of the carrier protein transthyretin display identical x-ray crystal structures to the wild-type protein and yet have substantially reduced thermodynamic stabilities (75). In such cases, a native-like conformation still represents the lowest energy state available; however, the free energy well in which this conformer sits is shallower due to a reduction in the number of stabilizing interactions. In the case of αHb, stabilization is provided by multiple subunit interactions in the tetramer.

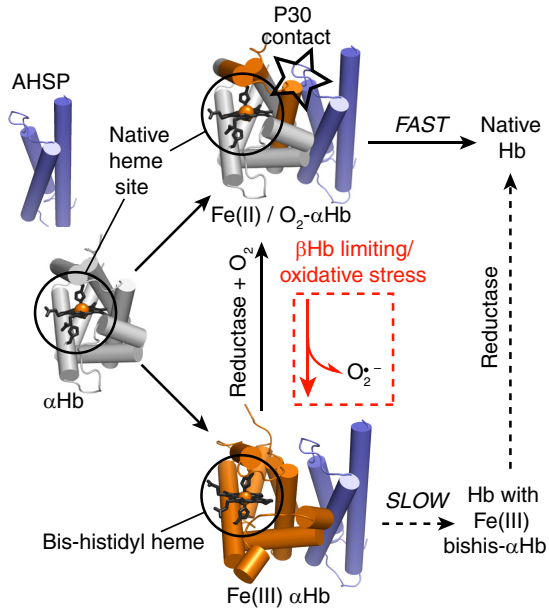

FIGURE 10. **Model for αHb·AHSP intermediates in Hb assembly.** Free αHb (*left*) has a native-like conformation (*gray color*). Pathways for incorporation of αHb into Hb are shown as *black arrows*. Deoxy Fe(II) αHb or O_2-αHb bind AHSP (*top row*) with a near-native structure and are rapidly combined with available βHb to produce native Hb. Fe(III) αHb binds AHSP in the high affinity bis-histidyl structure (*orange*, *bottom row*), inhibiting release of Fe(III) αHb to Hb. Methemoglobin reductase reduces bis-histidyl αHb to the native αHb structure. In Fe(II)/O_2-αHb·AHSP, interaction between AHSP Pro-30 and helix G of αHb (*star*) introduces strain in the proximal heme pocket (*orange shading*). Under conditions of limiting βHb or elevated redox stress, autooxidation of Fe(II)/O_2-αHb to the inert bis-histidyl complex occurs (*red arrows*).

CO- and O_2-Hb Have Native-like Conformations in Complex with AHSP—A previous x-ray crystallographic study from our group suggested that O_2-αHb underwent large conformational changes upon binding AHSP (1), and it was assumed that these changes were responsible for the accelerated autooxidation. In that study residues Asp-74–Leu-91 of αHb (helix F) appeared disordered (as judged from a lack of interpretable electron density), and the heme-ligating residue was switched from the usual His-87 in helix F to His-58 in helix E. However, NMR line shape and TALOS+ chemical shift data presented here show that, in the solution state, helix F retains an ordered α-helical structure in CO-αHb·AHSP. In addition, analysis of His side chain resonances strongly suggests that His-87 retains the heme binding role. In the crystal structure, the Fe-O_2 bond is unusually long (2.7 Å) (1). Such a long Fe-O_2 bond is inconsistent with visible absorption and XANES and EXAFS spectroscopic data (Table 3), which indicate that the iron coordination

geometries of O_2-αHb and O_2-αHb·AHSP are very similar. The EXAFS data do indicate a slight lengthening of the Fe-O_2 bond from 1.83 Å in O_2-αHb to 1.86 Å in O_2-αHb·AHSP, providing structural evidence that AHSP promotes superoxide dissociation and a decrease in O_2 affinity (Table 7).

Several possible explanations exist for the differences between the crystal structure described previously and the solution structure reported here. A detergent molecule located close to the heme group in the crystal might have influenced the structure; however, the detergent makes very few direct contacts with the protein. Perhaps more significantly, the crystals were grown under a standard atmosphere making it likely that partial autooxidation of αHb would occur. In addition, the intense x-ray beams used for protein crystallography can promote reduction of ferric proteins (59). A mixture of heme states arising from these processes would introduce static disorder in the crystal, complicating analysis of the x-ray data. Nevertheless, the crystal structure does provide evidence that helix F of αHb is susceptible to conformational distortion in the presence of AHSP.

AHSP Pro-30 Promotes Changes in the Proximal Heme Pocket of O_2-αHb That Enhance Autooxidation—We have previously shown that mutation of Pro-30 to a range of other residues types leads to a 4-fold reduction in autooxidation of αHb. Here we show that introducing Pro at other positions in loop 1 did not restore native O_2-αHb autooxidation and, although the $AHSP^{P30A/N28P}$ may undergo *cis*/*trans* isomerization, O_2-αHb autooxidation was not enhanced above the rate observed for $AHSP^{P30A}$, which is only 2–3-fold greater than that of free O_2-αHb (27). These data emphasize that the position of Pro-30 in AHSP loop 1 is critical to enhancing autooxidation.

AHSP Pro-30 is positioned adjacent to the beginning of helix G in the bis-histidyl αHb·AHSP complex. However, in the absence of crystallographic data, the degree of interaction between Pro-30 and helix G in O_2-αHb·AHSP is unknown. Based on mutation and binding data, which show that Pro-30 destabilizes the O_2-αHb·AHSP interface but not the bis-histidyl αHb·AHSP interface (11, 25, 27), we previously proposed that Pro-30 introduces a steric clash at the O_2-αHb·AHSP interface, which is relieved upon transition to the bis-histidyl αHb·AHSP structure. Here we show that AHSP binding induces NMR chemical shift perturbations in F, G, and H helices of CO-αHb, which constitute the proximal heme pocket, and that mutation of Pro-30 markedly reduces these disturbances. These findings are consistent with a steric interaction between AHSP Pro-30 and αHb helix G that is propagated through packing interactions of the F, G, and H helices (represented as *orange shading* of these helices in Fig. 10, *top row*). Bonding interactions between the heme iron and proximal His-87 in helix F and the geometry of the proximal pocket are important factors influencing ligand reactivity of the iron (76, 77). It is, therefore, significant that AHSP decreases O_2 affinity and CO association rates of αHb and that mutation of Pro-30 restores ligand reactivity of the heme iron to near-normal levels, which suggests strongly that Pro-30-induced disturbance of the proximal heme pocket contributes to enhanced O_2-αHb autooxidation and lower ligand reactivity in the presence of wild-type AHSP.

O_2-αHb·AHSP and Bis-histidyl·AHSP Intermediates in Hb Assembly—Our data suggest a model in which AHSP can bind αHb in one of two well ordered conformations depending on the oxidation/ligand state of the heme (Fig. 10). O_2-αHb is bound in a near-native conformation (Fig. 10, *top*), whereas Fe(III) αHb adopts a non-native globin conformation and bis-histidyl heme coordination (Fig. 10, *bottom*). We expect that Fe(II) deoxy αHb and CO-αHb will also bind to AHSP with near-native protein conformations on the basis that these forms of αHb all show the same affinity for AHSP as O_2-αHb, which is 100-fold weaker than the interaction of AHSP with the non-native bis-histidyl Fe(III) αHb conformation (20, 25, 27). Notably, deoxy-Fe(II) αHb does not adopt bis-histidyl heme coordination (26) despite the availability of an open iron axial coordination site. These studies emphasize that specific coordination between the distal His-58 and the Fe(III) iron center and the structural changes in the αHb polypeptide chain occur in a concerted fashion during oxidation of the αHb·AHSP complex and do not occur when the iron atom is reduced.

Based on kinetic data, Khandros *et al.* (11) and Mollan *et al.* (27) proposed that αHb synthesized in the Fe(III) form in the presence of AHSP (78) proceeds through a bis-histidyl αHb·AHSP folding intermediate before heme reduction and incorporation into Hb (Fig. 10, *solid black arrows*). Bis-histidyl ferric αHb can in principle be transferred to βHb and subsequently reduced (Fig. 10, *dashed arrows*); however, the rate of ferric αHb·AHSP dissociation is probably too slow to be physiologically relevant, and reduction almost certainly occurs more rapidly (27). Based on autooxidation rates measured *in vitro* (11, 20, 25, 28, 29), newly reduced Fe(II)/O_2-αHb should be rapidly incorporated into Hb before autooxidation can occur if the concentration of free βHb is high. However, under conditions of limiting βHb that are known to occur during normal erythropoiesis (79, 80), the likelihood increases for the conversion of Fe(II)/O_2-αHb·AHSP species to bis-histidyl ferric complexes (Fig. 10, *red arrows*). The more rapid autooxidation of αHb in the presence of AHSP may be advantageous, as it provides a means to trap αHb in a relatively unreactive Fe(III) state that inhibits redox cycling and reactions with reactive oxygen species that could otherwise occur with free αHb. In addition, both free O_2-αHb and met-Hb subunits are more prone to H_2O_2-induced ferryl and protein radical formation and precipitation (20, 81), making it advantageous to remove free O_2-αHb and stabilize it as bis-histyl met-αHb·AHSP under conditions of oxidative stress.

To investigate the biological importance of autooxidation rate, Khandros *et al.* (11) performed gene knock-in experiments in mice. Mutations of AHSP Pro-30 to Ala or Trp did not disturb erythropoiesis (11), which suggested that a 4-fold decrease in αHb·AHSP autooxidation rate is not sufficient to elicit changes in erythropoiesis in the normal mouse model (11, 27). However, it is important to recognize that O_2-αHb·$AHSP^{P30A}$ still autooxidizes more quickly than does free O_2-αHb (11, 25, 27) and that other interactions across the αHb·AHSP interface, in addition to those with Pro-30, are important for autooxidation and hemichrome formation.

A transition between two metastable αHb·AHSP structures, as outlined in Fig. 10, avoids persistent disordered states that

would favor unregulated reactions with an exposed heme and rapid heme dissociation. In this regard, it is interesting that mutations of Pro-30 to Ala or Trp decrease O_2-αHb autooxidation rates but enhance heme dissociation rates (11). In conclusion, it appears that the AHSP sequence has evolved to achieve a fine balance of distorting αHb sufficiently to promote changes in heme coordination that inhibit reactions with H_2O_2 without inducing an unacceptably high risk of heme loss or other irreversible denaturation events.

A Physiological Role for O_2-αHb·AHSP beyond the Red Blood Cell—Recently Straub *et al.* (82) reported that αHb and AHSP (but not βHb) are expressed in arterial endothelial cells at sites where the endothelial cells make direct contact with underlying smooth muscle (myoendothelial junctions) and that αHb expression regulates NO signaling from the endothelium to smooth muscle. NO signaling is important for maintaining vascular tone and modulating the response of smooth muscle to vasodilator and vasoconstrictor messengers. Importantly, the effect of heme proteins on NO signaling is dependent on the iron oxidation and ligand state. Fe(III) heme interacts only very weakly with NO, providing no barrier to NO diffusion. In contrast, O_2-heme reacts rapidly with NO to form nitrate (NO_3^-) and Fe(III) heme, thus quenching NO signaling (83–85). In the endothelium, the reaction of NO with O_2-αHb·AHSP is expected to generate bis-histidyl αHb·AHSP. Therefore, in endothelial cells the balance between O_2-αHb·AHSP and Fe(III) bis-histidyl αHb·AHSP will impose restrictive/permissive states for NO signaling, respectively. In this regard, autooxidation and the interaction of Fe(III) bis-histidyl αHb·AHSP with reductase systems in endothelial cells are critical processes. Understanding these processes is now necessary for a full understanding of NO signaling in the vasculature.

Acknowledgments—We thank Dr. Chien Ho for the kind gift of the pHE7 plasmid and Drs. Aviva Levina, Hugh Harris, Matthew Latimer, and Allyson Soo Hoo for assistance at Stanford Synchrotron Radiation Lightsource. This work was performed with support from the Australian Synchrotron Research Program, which was funded by the Commonwealth of Australia under the Major National Research Facilities Program. Portions of this research were carried out at the Stanford Synchrotron Radiation Lightsource. The Stanford Synchrotron Radiation Lightsource Structural Molecular Biology Program is supported by the Department of Energy, Office of Biological and Environmental Research, and by the National Institutes of Health, National Center for Research Resources, Biomedical Technology Program.

REFERENCES

1. Feng, L., Gell, D. A., Zhou, S., Gu, L., Kong, Y., Li, J., Hu, M., Yan, N., Lee, C., Rich, A. M., Armstrong, R. S., Lay, P. A., Gow, A. J., Weiss, M. J., Mackay, J. P., and Shi, Y. (2004) Molecular mechanism of AHSP-mediated stabilization of α-hemoglobin. *Cell* **119,** 629–640
2. Feng, L., Zhou, S., Gu, L., Gell, D. A., Mackay, J. P., Weiss, M. J., Gow, A. J., and Shi, Y. (2005) Structure of oxidized α-haemoglobin bound to AHSP reveals a protective mechanism for haem. *Nature* **435,** 697–701
3. Gell, D., Kong, Y., Eaton, S. A., Weiss, M. J., and Mackay, J. P. (2002) Biophysical characterization of the α-globin binding protein α-hemoglobin stabilizing protein. *J. Biol. Chem.* **277,** 40602–40609
4. Kihm, A. J., Kong, Y., Hong, W., Russell, J. E., Rouda, S., Adachi, K., Simon, M. C., Blobel, G. A., and Weiss, M. J. (2002) An abundant erythroid protein that stabilizes free α-haemoglobin. *Nature* **417,** 758–763
5. dos Santos, C. O., Duarte, A. S., Saad, S. T., and Costa, F. F. (2004) Expression of α-hemoglobin stabilizing protein gene during human erythropoiesis. *Exp. Hematol.* **32,** 157–162
6. Kong, Y., Zhou, S., Kihm, A. J., Katein, A. M., Yu, X., Gell, D. A., Mackay, J. P., Adachi, K., Foster-Brown, L., Louden, C. S., Gow, A. J., and Weiss, M. J. (2004) Loss of α-hemoglobin-stabilizing protein impairs erythropoiesis and exacerbates β-thalassemia. *J. Clin. Invest.* **114,** 1457–1466
7. Lai, M. I., Jiang, J., Silver, N., Best, S., Menzel, S., Mijovic, A., Colella, S., Ragoussis, J., Garner, C., Weiss, M. J., and Thein, S. L. (2006) α-Haemoglobin stabilising protein is a quantitative trait gene that modifies the phenotype of β-thalassaemia. *Br. J. Haematol.* **133,** 675–682
8. Giordano, P. C., Zweegman, S., Akkermans, N., Arkesteijn, S. G., van Delft, P., Versteegh, F. G., Wajcman, H., and Harteveld, C. L. (2007) The first case of Hb Groene Hart [α119(H2)Pro→Ser, CCT→TCT (α1)] homozygosity confirms that α thalassemia phenotype is associated with this abnormal hemoglobin variant. *Hemoglobin* **31,** 179–182
9. Yu, X., Kong, Y., Dore, L. C., Abdulmalik, O., Katein, A. M., Zhou, S., Choi, J. K., Gell, D., Mackay, J. P., Gow, A. J., and Weiss, M. J. (2007) An erythroid chaperone that facilitates folding of α-globin subunits for hemoglobin synthesis. *J. Clin. Invest.* **117,** 1856–1865
10. Nasimuzzaman, M., Khandros, E., Wang, X., Kong, Y., Zhao, H., Weiss, D., Rivella, S., Weiss, M. J., and Persons, D. A. (2010) Analysis of α hemoglobin stabilizing protein overexpression in murine β-thalassemia. *Am. J. Hematol.* **85,** 820–822
11. Khandros, E., Mollan, T. L., Yu, X., Wang, X., Yao, Y., D'Souza, J., Gell, D. A., Olson, J. S., and Weiss, M. J. (2012) Insights into hemoglobin assembly through *in vivo* mutagenesis of α-hemoglobin stabilizing protein. *J. Biol. Chem.* **287,** 11325–11337
12. Yu, X., Mollan, T. L., Butler, A., Gow, A. J., Olson, J. S., and Weiss, M. J. (2009) Analysis of human α globin gene mutations that impair binding to the α hemoglobin stabilizing protein. *Blood* **113,** 5961–5969
13. Giulivi, C., and Davies, K. J. (1994) Hydrogen peroxide-mediated ferrylhemoglobin generation *in vitro* and in red blood cells. *Methods Enzymol.* **231,** 490–496
14. Nagababu, E., and Rifkind, J. M. (2000) Reaction of hydrogen peroxide with ferrylhemoglobin. Superoxide production and heme degradation. *Biochemistry* **39,** 12503–12511
15. Reeder, B. J., Svistunenko, D. A., Cooper, C. E., and Wilson, M. T. (2004) The radical and redox chemistry of myoglobin and hemoglobin. From *in vitro* studies to human pathology. *Antioxid. Redox. Signal* **6,** 954–966
16. Svistunenko, D. A. (2005) Reaction of haem containing proteins and enzymes with hydroperoxides. The radical view. *Biochim. Biophys. Acta* **1707,** 127–155
17. Reeder, B. J. (2010) The redox activity of hemoglobins. From physiologic functions to pathologic mechanisms. *Antioxid. Redox. Signal* **13,** 1087–1123
18. Joshi, W., Leb, L., Piotrowski, J., Fortier, N., and Snyder, L. M. (1983) Increased sensitivity of isolated α subunits of normal human hemoglobin to oxidative damage and crosslinkage with spectrin. *J. Lab. Clin. Med.* **102,** 46–52
19. Scott, M. D., van den Berg, J. J., Repka, T., Rouyer-Fessard, P., Hebbel, R. P., Beuzard, Y., and Lubin, B. H. (1993) Effect of excess α-hemoglobin chains on cellular and membrane oxidation in model β-thalassemic erythrocytes. *J. Clin. Invest.* **91,** 1706–1712
20. Mollan, T. L., Banerjee, S., Wu, G., Parker Siburt, C. J., Tsai, A. L., Olson, J. S., Weiss, M. J., Crumbliss, A. L., and Alayash, A. I. (2013) α-Hemoglobin stabilizing protein (AHSP) markedly decreases the redox potential and reactivity of α subunits of human HbA with hydrogen peroxide. *J. Biol. Chem.* **288,** 4288–4298
21. Amer, J., Goldfarb, A., and Fibach, E. (2003) Flow cytometric measurement of reactive oxygen species production by normal and thalassaemic red blood cells. *Eur. J. Haematol.* **70,** 84–90
22. Srinoun, K., Svasti, S., Chumworathayee, W., Vadolas, J., Vattanaviboon, P., Fucharoen, S., and Winichagoon, P. (2009) Imbalanced globin chain synthesis determines erythroid cell pathology in thalassemic mice. *Haematologica* **94,** 1211–1219
23. Leecharoenkiat, A., Wannatung, T., Lithanatudom, P., Svasti, S., Fucha-

roen, S., Chokchaichamnankit, D., Srisomsap, C., and Smith, D. R. (2011) Increased oxidative metabolism is associated with erythroid precursor expansion in β^0-thalassaemia/Hb E disease. *Blood Cells Mol. Dis.* **47,** 143–157
24. De Franceschi, L., Bertoldi, M., De Falco, L., Santos Franco, S., Ronzoni, L., Turrini, F., Colancecco, A., Camaschella, C., Cappellini, M. D., and Iolascon, A. (2011) Oxidative stress modulates heme synthesis and induces peroxiredoxin-2 as a novel cytoprotective response in β-thalassemic erythropoiesis. *Haematologica* **96,** 1595–1604
25. Gell, D. A., Feng, L., Zhou, S., Jeffrey, P. D., Bendak, K., Gow, A., Weiss, M. J., Shi, Y., and Mackay, J. P. (2009) A *cis*-proline in α-hemoglobin stabilizing protein directs the structural reorganization of α-hemoglobin. *J. Biol. Chem.* **284,** 29462–29469
26. Hamdane, D., Vasseur-Godbillon, C., Baudin-Creuza, V., Hoa, G. H., and Marden, M. C. (2007) Reversible hexacoordination of α-hemoglobin-stabilizing protein (AHSP)/α-hemoglobin *versus* pressure. Evidence for protection of the α-chains by their chaperone. *J. Biol. Chem.* **282,** 6398–6404
27. Mollan, T. L., Khandros, E., Weiss, M. J., and Olson, J. S. (2012) The kinetics of α-globin binding to α hemoglobin stabilizing protein (AHSP) indicate preferential stabilization of a hemichrome folding intermediate. *J. Biol. Chem.* **287,** 11338–11350
28. Vasseur-Godbillon, C., Hamdane, D., Marden, M. C., and Baudin-Creuza, V. (2006) High-yield expression in *Escherichia coli* of soluble human α-hemoglobin complexed with its molecular chaperone. *Protein Eng. Des. Sel.* **19,** 91–97
29. Zhou, S., Olson, J. S., Fabian, M., Weiss, M. J., and Gow, A. J. (2006) Biochemical fates of α hemoglobin bound to α-hemoglobin-stabilizing protein AHSP. *J. Biol. Chem.* **281,** 32611–32618
30. Simplaceanu, V., Lukin, J. A., Fang, T. Y., Zou, M., Ho, N. T., and Ho, C. (2000) Chain-selective isotopic labeling for NMR studies of large multimeric proteins. Application to hemoglobin. *Biophys. J.* **79,** 1146–1154
31. Looker, D., Mathews, A. J., Neway, J. O., and Stetler, G. L. (1994) Expression of recombinant human hemoglobin in *Escherichia coli*. *Methods Enzymol.* **231,** 364–374
32. Cai, M., Huang, Y., Sakaguchi, K., Clore, G. M., Gronenborn, A. M., and Craigie, R. (1998) An efficient and cost-effective isotope labeling protocol for proteins expressed in *Escherichia coli*. *J. Biomol. NMR* **11,** 97–102
33. Shen, T. J., Ho, N. T., Zou, M., Sun, D. P., Cottam, P. F., Simplaceanu, V., Tam, M. F., Bell, D. A., Jr., and Ho, C. (1997) Production of human normal adult and fetal hemoglobins in *Escherichia coli*. *Protein Eng.* **10,** 1085–1097
34. Gill, S. C., and von Hippel, P. H. (1989) Calculation of protein extinction coefficients from amino acid sequence data. *Anal. Biochem.* **182,** 319–326
35. Eaton, W. A., and Hofrichter, J. (1981) Polarized absorption and linear dichroism spectroscopy of hemoglobin. *Methods Enzymol.* **76,** 175–261
36. Folta-Stogniew, E., and Williams, K. R. (1999) Determination of molecular masses of proteins in solution. Implementation of an HPLC size exclusion chromatography and laser light scattering service in a core laboratory. *J. Biomol. Tech.* **10,** 51–63
37. Goddard, T. D., and Kneller, D. G. (2006) SPARKY, University of California at San Francisco
38. Pelton, J. G., Torchia, D. A., Meadow, N. D., and Roseman, S. (1993) Tautomeric states of the active-site histidines of phosphorylated and unphosphorylated IIIGlc, a signal-transducing protein from *Escherichia coli*, using two-dimensional heteronuclear NMR techniques. *Protein Sci.* **2,** 543–558
39. Cramer, S. P., Tench, O., Yocum, M., and George, G. N. (1988) A 13-element Ge detector for fluorescence EXAFS. *Nucl. Instrum. Methods Phys. Res. A* **266,** 586–591
40. Zhang, Y., Pavlosky, M. A., Brown, C. A., Westre, T. E., Hedman, B., Hodgson, K. O., and Solomon, E. I. (1992) Spectroscopic and theoretical description of the electronic structure of the S = 3/2 nitrosyl complex of non-heme iron enzymes. *J. Am. Chem. Soc.* **114,** 9189–9191
41. Rich, A. M., Armstrong, R. S., Ellis, P. J., Freeman, H. C., and Lay, P. A. (1998) Determination of iron-ligand bond lengths in horse heart met- and deoxymyoglobin using multiple-scattering XAFS analyses. *Inorg. Chem.* **37,** 5743–5753
42. Ellis, P. J., and Freeman, H. C. (1995) XFIT. An interactive EXAFS analysis program. *J. Synchrotron. Radiat.* **2,** 190–195
43. Jameson, G. B., Molinaro, F. S., Ibers, J. A., Collman, J. P., Brauman, J. I., Rose, E., and Suslick, K. S. (1980) Models for the active site of oxygen-binding hemoproteins. Dioxygen binding properties and the structures of (2-methylimidazole)-meso-tetra(α,α,α,α-*o*-pivalamidophenyl)porphyrinatoiron(II)-ethanol and its dioxygen adduct. *J. Am. Chem. Soc.* **102,** 3224–3237
44. Penner-Hahn, J. (2004) in *Comprehensive Coordination Chemistry II; From Biology to Nanotechnology* (Lever, A. B. P., ed.) pp. 159, Elsevier, Oxford
45. Birukou, I., Schweers, R. L., and Olson, J. S. (2010) Distal histidine stabilizes bound O_2 and acts as a gate for ligand entry in both subunits of adult human hemoglobin. *J. Biol. Chem.* **285,** 8840–8854
46. Santiveri, C. M., Pérez-Cañadillas, J. M., Vadivelu, M. K., Allen, M. D., Rutherford, T. J., Watkins, N. A., and Bycroft, M. (2004) NMR structure of the α-hemoglobin stabilizing protein. Insights into conformational heterogeneity and binding. *J. Biol. Chem.* **279,** 34963–34970
47. Martineau, L., and Craescu, C. T. (1992) Sequential assignment of the proton NMR spectrum of isolated α(CO) chains from human adult hemoglobin. *Eur. J. Biochem.* **205,** 661–670
48. Antonini, E., Bucci, E., Fronticelli, C., Chiancone, E., Wyman, J., and Rossi-Fanelli, A. (1966) The properties and interactions of the isolated α- and β-chains of human haemoglobin. V. The reaction of α- and β-chains. *J. Mol. Biol.* **17,** 29–46
49. Valdes, R., Jr., and Ackers, G. K. (1977) Thermodynamic studies on subunit assembly in human hemoglobin. Self-association of oxygenated chains (αSH and βSH). Determination of stoichiometries and equilibrium constants as a function of temperature. *J. Biol. Chem.* **252,** 74–81
50. Bucci, E., and Fronticelli, C. (1965) A new method for the preparation of α and β subunits of human hemoglobin. *J. Biol. Chem.* **240,** PC551–552
51. Brunori, M., Noble, R. W., Antonini, E., and Wyman, J. (1966) The reactions of the isolated α and β chains of human hemoglobin with oxygen and carbon monoxide. *J. Biol. Chem.* **241,** 5238–5243
52. Shen, Y., Delaglio, F., Cornilescu, G., and Bax, A. (2009) TALOS+. A hybrid method for predicting protein backbone torsion angles from NMR chemical shifts. *J. Biomol. NMR* **44,** 213–223
53. Park, S. Y., Yokoyama, T., Shibayama, N., Shiro, Y., and Tame, J. R. (2006) 1.25 Å resolution crystal structures of human haemoglobin in the oxy-, deoxy-, and carbonmonoxy forms. *J. Mol. Biol.* **360,** 690–701
54. Kabsch, W., and Sander, C. (1983) Dictionary of protein secondary structure. Pattern recognition of hydrogen-bonded and geometrical features. *Biopolymers* **22,** 2577–2637
55. Dalvit, C., Tennant, L., and Wright, P. E. (1987) ^{1}H resonances of proximal histidine in CO complexes of hemoglobins provide a sensitive probe of coordination geometry. *FEBS Lett.* **213,** 289–292
56. Dalvit, C., and Wright, P. E. (1987) Assignment of resonances in the ^{1}H nuclear magnetic resonance spectrum of the carbon monoxide complex of human hemoglobin α-chains. *J. Mol. Biol.* **194,** 329–339
57. Lukin, J. A., Simplaceanu, V., Zou, M., Ho, N. T., and Ho, C. (2000) NMR reveals hydrogen bonds between oxygen and distal histidines in oxyhemoglobin. *Proc. Natl. Acad. Sci. U.S.A.* **97,** 10354–10358
58. Levina, A., Armstrong, R. S., and Lay, P. A. (2005) Three-dimensional structure determination using multiple-scattering analysis of XAFS. Applications to metalloproteins and coordination chemistry. *Coord. Chem. Rev.* **249,** 141–160
59. George, G. N., Pickering, I. J., Pushie, M. J., Nienaber, K., Hackett, M. J., Ascone, I., Hedman, B., Hodgson, K. O., Aitken, J. B., Levina, A., Glover, C., and Lay, P. A. (2012) X-ray-induced photo-chemistry and X-ray absorption spectroscopy of biological samples. *J. Synchrotron. Radiat.* **19,** 875–886
60. Rich, A. M. (1997) *Determination of Fe-ligand bond lengths and angles in hemeproteins using x-ray absorption Spectroscopy*. Ph.D thesis, School of Chemistry, The University of Sydney, Sydney
61. Reed, C. A., and Cheung, S. K. (1977) On the bonding of FeO_2 in hemoglobin and related dioxygen complexes. *Proc. Natl. Acad. Sci. U.S.A.* **74,** 1780–1784
62. Spiro, T. G., and Strekas, T. C. (1974) Resonance Raman spectra of heme proteins. Effects of oxidation and spin state. *J. Am. Chem. Soc.* **96,** 338–345

63. Binsted, N., Strange, R. W., and Hasnain, S. S. (1992) Constrained and restrained refinement in EXAFS data analysis with curved wave theory. *Biochemistry* **31,** 12117–12125
64. Chance, M. R., Miller, L. M., Fischetti, R. F., Scheuring, E., Huang, W. X., Sclavi, B., Hai, Y., and Sullivan, M. (1996) Global mapping of structural solutions provided by the extended x-ray absorption fine structure ab initio code FEFF 6.01. Structure of the cryogenic photoproduct of the myoglobin-carbon monoxide complex. *Biochemistry* **35,** 9014–9023
65. Hasnain, S. S., and Hodgson, K. O. (1999) Structure of metal centres in proteins at subatomic resolution. *J. Synchrotron Radiat.* **6,** 852–864
66. Rich, A. M., Armstrong, R. S., Ellis, P. J., and Lay, P. A. (1998) Determination of the Fe-ligand bond lengths and Fe-N-O bond angles in horse heart ferric and ferrous nitrosylmyoglobin using multiple-scattering XAFS analyses. *J. Am. Chem. Soc.* **120,** 10827–10836
67. Vojtechovský, J., Chu, K., Berendzen, J., Sweet, R. M., and Schlichting, I. (1999) Crystal structures of myoglobin-ligand complexes at near-atomic resolution. *Biophys. J.* **77,** 2153–2174
68. Kachalova, G. S., Popov, A. N., and Bartunik, H. D. (1999) A steric mechanism for inhibition of CO binding to heme proteins. *Science* **284,** 473–476
69. Li, R., Nagai, Y., and Nagai, M. (2000) Changes of tyrosine and tryptophan residues in human hemoglobin by oxygen binding. Near- and far-UV circular dichroism of isolated chains and recombined hemoglobin. *J. Inorg. Biochem.* **82,** 93–101
70. Beychok, S., Tyuma, I., Benesch, R. E., and Benesch, R. (1967) Optically active absorption bands of hemoglobin and its subunits. *J. Biol. Chem.* **242,** 2460–2462
71. Geraci, G., and Li, T. K. (1969) Circular dichroism of isolated and recombined hemoglobin chains. *Biochemistry* **8,** 1848–1854
72. Geraci, G., and Parkhurst, L. J. (1981) Circular dichroism spectra of hemoglobins. *Methods Enzymol.* **76,** 262–275
73. Tran, A. T., Kolczak, U., and La Mar, G. N. (2003) Solution ^{1}H NMR study of the active site molecular structure and magnetic properties of the cyanomet complex of the isolated α-chain from human hemoglobin A. *Biochim. Biophys. Acta* **1650,** 59–72
74. Tran, A. T., Kolczak, U., and La Mar, G. N. (2004) Solution ^{1}H NMR study of the active site molecular structure and magnetic properties of the cyanomet complex of the isolated, tetrameric β-chain from human adult hemoglobin. *Biochim. Biophys. Acta* **1701,** 75–87
75. Azevedo, E. P., Pereira, H. M., Garratt, R. C., Kelly, J. W., Foguel, D., and Palhano, F. L. (2011) Dissecting the structure, thermodynamic stability, and aggregation properties of the A25T transthyretin (A25T-TTR) variant involved in leptomeningeal amyloidosis. Identifying protein partners that co-aggregate during A25T-TTR fibrillogenesis in cerebrospinal fluid. *Biochemistry* **50,** 11070–11083
76. Olson, J. S., and Phillips, G. N., Jr. (1997) Myoglobin discriminates between O_2, NO, and CO by electrostatic interactions with the bound ligand. *J. Biol. Inorg. Chem.* **2,** 544–552
77. Capece, L., Marti, M. A., Crespo, A., Doctorovich, F., and Estrin, D. A. (2006) Heme protein oxygen affinity regulation exerted by proximal effects. *J. Am. Chem. Soc.* **128,** 12455–12461
78. Schulman, H. M., Martinez-Medellin, J., and Sidloi, R. (1974) The oxidation state of newly synthesized hemoglobin. *Biochem. Biophys. Res. Commun.* **56,** 220–226
79. Gill, F. M., and Schwartz, E. (1973) Free α-globin pool in human bone marrow. *J. Clin. Invest.* **52,** 3057–3063
80. Vasseur, C., Pissard, S., Domingues-Hamdi, E., Marden, M. C., Galactéros, F., and Baudin-Creuza, V. (2011) Evaluation of the free α-hemoglobin pool in red blood cells. A new test providing a scale of β-thalassemia severity. *Am. J. Hematol.* **86,** 199–202
81. Tomoda, A., Sugimoto, K., Suhara, M., Takeshita, M., and Yoneyama, Y. (1978) Haemichrome formation from haemoglobin subunits by hydrogen peroxide. *Biochem. J.* **171,** 329–335
82. Straub, A. C., Lohman, A. W., Billaud, M., Johnstone, S. R., Dwyer, S. T., Lee, M. Y., Bortz, P. S., Best, A. K., Columbus, L., Gaston, B., and Isakson, B. E. (2012) Endothelial cell expression of haemoglobin α regulates nitric oxide signalling. *Nature* **491,** 473–477
83. Doherty, D. H., Doyle, M. P., Curry, S. R., Vali, R. J., Fattor, T. J., Olson, J. S., and Lemon, D. D. (1998) Rate of reaction with nitric oxide determines the hypertensive effect of cell-free hemoglobin. *Nat. Biotechnol.* **16,** 672–676
84. Eich, R. F., Li, T., Lemon, D. D., Doherty, D. H., Curry, S. R., Aitken, J. F., Mathews, A. J., Johnson, K. A., Smith, R. D., Phillips, G. N., Jr., and Olson, J. S. (1996) Mechanism of NO-induced oxidation of myoglobin and hemoglobin. *Biochemistry* **35,** 6976–6983
85. Kim-Shapiro, D. B., Schechter, A. N., and Gladwin, M. T. (2006) Unraveling the reactions of nitric oxide, nitrite, and hemoglobin in physiology and therapeutics. *Arterioscler. Thromb. Vasc. Biol.* **26,** 697–705